TIME DOMAIN TERAHERTZ ATTENUATED TOTAL INTERNAL REFLECTION SPECTROSCOPY

A THESIS SUBMITTED TO
THE GRADUATE SCHOOL OF NATURAL AND APPLIED SCIENCES
OF
MIDDLE EAST TECHNICAL UNIVERSITY

BY

ATABERK ATALAR

IN PARTIAL FULFILLMENT OF THE REQUIREMENTS
FOR
THE DEGREE OF MASTER OF SCIENCE
IN
PHYSICS

JULY 2021

Approval of the thesis:

TIME DOMAIN TERAHERTZ ATTENUATED TOTAL INTERNAL REFLECTION SPECTROSCOPY

submitted by **ATABERK ATALAR** in partial fulfillment of the requirements for the degree of **Master of Science in Physics Department, Middle East Technical University** by,

Prof. Dr. Halil Kalıpçılar
Dean, Graduate School of **Natural and Applied Sciences** _____

Prof. Dr. Seçkin Kürkçüoğlu
Head of Department, **Physics** _____

Prof. Dr. Hakan Altan
Supervisor, **Physics, METU** _____

Examining Committee Members:

Prof. Dr. Asaf Behzat Şahin
Electrical Engineering, Yıldırım Beyazıt University _____

Prof. Dr. Hakan Altan
Physics, METU _____

Assoc. Prof. Dr. Alpan Bek
Physics, METU _____

Date: 30.07.2021

I hereby declare that all information in this document has been obtained and presented in accordance with academic rules and ethical conduct. I also declare that, as required by these rules and conduct, I have fully cited and referenced all material and results that are not original to this work.

Name, Surname: Ataberk Atalar

Signature :

ABSTRACT

TIME DOMAIN TERAHERTZ ATTENUATED TOTAL INTERNAL REFLECTION SPECTROSCOPY

Atalar, Ataberk
M.S., Department of Physics
Supervisor: Prof. Dr. Hakan Altan

July 2021, 78 pages

In this thesis, a Terahertz Time Domain Spectroscopy system based on the Attenuated Total Internal Reflection principle (THz ATR-TDS) was constructed in order to non-destructively evaluate materials which show high absorptive characteristics at THz frequencies and therefore prove other widely used THz transmission spectroscopy methods ineffective. The response of the system without a sample differ in amplitude and in time scale when compared to a sample measurement due to the real and imaginary parts of the refractive index of the samples. Through an analysis of the interaction of the THz field with the sample and signal processing in time and frequency domain, optical properties of samples in the THz frequency range were obtained. THz signal was generated and detected by two InGaAs based photoconductive antennas (PCA) and a bandwidth up to 1 THz was obtained. Generated THz beam was guided by off-axis parabolic mirrors and then focused inside a Si (Silicon) prism to reflect internally at the base with an incidence angle of 51.6° according to total internal reflection (TIR) principle. The diameter of the focal point at this surface was measured to be 4 mm. Measurements of water which has an exceptionally high absorption in THz region of electromagnetic spectrum were presented in order

to assess the effectiveness of the constructed spectroscopy system. In addition, mouth tissue samples with different types of lesions prepared by the Faculty of Dentistry of Ankara University in Ankara, Turkey were investigated to determine the efficiency of the THz ATR-TDS technique in analysis of biological samples which contain high amount of water. It has been shown that by using this system, high absorptive materials such as water and other various water containing samples could be optically characterized at THz frequencies through time and frequency domain analysis.

Keywords: Terahertz Time Domain Spectroscopy, Therahertz ATR Spectroscopy, Attenuated Total Internal Reflection, Total Internal Reflection

ÖZ

ZAMANA DAYALI TERAHERTZ AZALAN TOPLAM İÇ YANSIMA SPEKTROSKOPİSİ

Atalar, Ataberk
Yüksek Lisans, Fizik Bölümü
Tez Yöneticisi: Prof. Dr. Hakan Altan

Temmuz 2021 , 78 sayfa

Bu tezde, Terahertz frekansında yüksek soğurucu özellikler gösteren ve bundan dolayı diğer yaygın olarak kullanılan geçişli teraherz spektroskopi tekniklerini etkisiz kılan materyalleri zararsız (yıkıcı olmayan) bir şekilde incelemek için Azalan Toplam İç Yansıma prensibini temel alarak bir Zamana Dayalı Terahertz Spekstroskopi sistemi kurulmuştur. Sistemin örneksiz ölçüm yanıtı ve örnekli ölçüm yanıtı karşılaştırıldığında kullanılan örneklerin kırıcılık indislerinin gerçek ve sanal kısımları dolayısıyla zaman ve büyüklük ölçeklerinde farklılıklar oluşmaktadır. Zamana ve frekansa dayalı bir dizi sinyal işleme ve matematiksel hesap serisinin ardından örneklerin optik özellikleri elde edilmiştir. THz sinyali iki InGaAs fotoiletken anten vasıtası ile üretilmiş ve tespit edilmiştir. Sistem bant genişliği 1 THz olarak ölçülmüştür. Üretilen THz ışını eksendışı parabolik aynalar ile yönledirilmiş ve bir Silikon (Si) prizmanın içerisine doğru, prizma tabanında iç yansıma elde edecek şekilde odaklanarak gönderilmiştir. Işının prizma tabanına geliş açısı $51.6°$ dir. Tabanda odaklanan ışığın odak nokta çapı 4 mm olarak ölçülmüştür. Sistemin etkinliğini ölçmek için elektromanyetik spektrumun THz bölgesinde istisnai derecede yüksek soğuruculuk gösteren su

incelemiş ve sonuçları sunulmuştur. Ek olarak, Ankara Üniversitesi Diş Hekimliği Fakültesi tarafından hazırlanan ve içlerinde farklı lezyonlar barındıran ağız doku örnekleri de THz-ATR tekniğinin yüksek oranda su içeren biyolojik örneklerin analizindeki performansını değerlendirmek amacıyla incelenmiştir. Sonuç olarak, bu sistem kullanılarak yüksek soğurucu özellikler gösteren su ve su içeren diğer materyallerin de terahertz frekansında zaman ve frekans uzayı analizi ile optik karakerizasyonunun yapılabileceği gösterilmiştir.

Anahtar Kelimeler: Zamana Dayalı Terahertz Spektroskopisi, Terahertz ATY Spektroskopisi, Azalan Toplam İç Yansıma, Toplam İç Yansıma

To my family and my cat.

ACKNOWLEDGMENTS

I am very grateful to my supervisor Prof. Hakan Altan for his guidance. His never ending patience and support was what made me and this research reach to this point.

I would also like to present my sincere thanks to Prof. Asaf Behzat Şahin for his continuous assistance throughout my research.

I would like to thank my friends from Physics department too for all the great memories throughout my undergraduate and graduate education.

Special thanks goes to my family for their endless support, love and encouragement.

This research is sponsored by TUBITAK (Scientific and Technological Research Council of Turkey) under project number 119S623.

TABLE OF CONTENTS

LIST OF FIGURES

FIGURES

LIST OF ABBREVIATIONS

ATR	Attenuated total (internal) reflection
EM	Electromagnetic
EO	Electro optical
Fs	Femtosecond
FTIR	Fourier transform infrared
FWHM	Full width at half maximum
GaP	Gallium phosphide
GaSe	Gallium selenide
HRFZ-Si	High resistivity float zone silicon
InP	Indium phosphide
IR	Infrared
$LiNbO_3$	Lithium niobate
PCA	Photoconducting antenna
Ps	Picosecond
SC	Semiconductor
SI	International system of units
GaAs	Gallium arsenide
SNR	Signal to noise ratio
TES	Terahertz emission spectroscopy
THz	Terahertz
THz-TDS	Terahertz time domain spectroscopy
TRTS	Time-resolved terahertz spectroscopy
ZnTe	Zinc telluride
Si	Silicon

Er	Erbium
Hz	Hertz
2D	2 Dimensional
3D	3 Dimensional
Yb	Ytterbium
GaBiAs	Gallium bismuth arsenide
OPL	Optical path length

CHAPTER 1

INTRODUCTION

The invisible portion of the electromagnetic spectrum has been of a great interest since the discovery of IR and UV regions by Willam Herschel and Johann Wilhelm Ritter in the very beginning of the 19th century [5][6]. However, although there have been studies which include THz region or as it was traditionally called far-infrared region towards the beginning of the 20th century, terahertz region alone has become an active area of investigation for the last three decades after achieving coherent THz radiation alongside with the invention of ultrafast lasers [7].

The name terahertz indicates a multiplication of one Hertz by 10^{12}. In other words, 1 THz is equal to 10^{12} Hertz or one trillion oscillations of electric and magnetic fields in one second. In electromagnetic (EM) spectrum, terahertz range lies between long wave infrared (IR) and microwave regions. The lowest THz frequency is accepted to be 100 GHz and the upper boundary expands up to 10 THz [8]. In terms of wavelength, the THz region is between 3 mm to 30 μm.

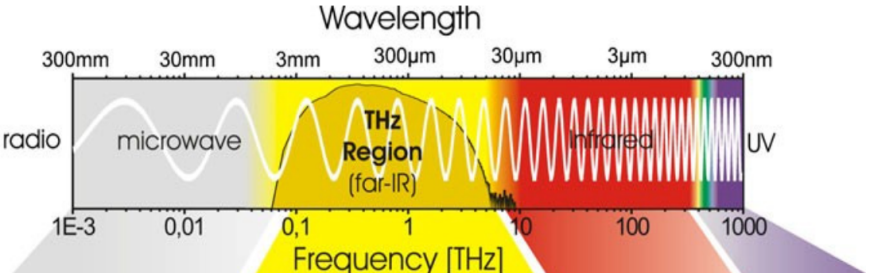

Figure 1.1: THz region in electromagnetic spectrum [1].

In vacuum of space, an electromagnetic wave with a frequency of 1 THz has a period of 1 ps and a wavenumber of 33 cm^{-1}. The corresponded wavelength is 300 μm. The

energy of photons at this frequency is equal to 4.1 meV and the equivalent temperature value is 47.6 K.

In electromagnetic spectrum, low frequency regions allow circuit systems to operate almost ideally. As the frequency value increases, certain limitations start to apply such as circuit sizes being comparable to wavelength values and application of transmission lines [9]. In microwave region, radiation begins to affect systems and a need for new approaches in circuit design arises. Going further from microwaves to THz region makes it almost impossible to construct a small enough circuit [10]. Therefore, in order to control EM radiation, different methods of manipulation which start to transit from electronics towards optics is required [11].

There has been a rise in the interest in discovering the bridge between the electric and IR waves around 1920s but standing between the borders of optics and electronics has made THz region of the spectrum difficult to explore [12]. Even after its discovery, not being able to provide efficient detectors and generators has turned terahertz into a complicated research area in terms of applications. As a result, THz region was nearly untouched for decades and it began to be called "THz gap".

The limitations in technology and difficulties in research did not stop scientists to aim their focus to THz region once again as they explored the neighboring regions more. Every new advancement in IR and microwave research opened a new door in THz research and revealed its unique nature [13].

Various molecules show high absorption and reveal absorption lines at THz frequencies. These absorption lines are specific to each molecule and can be imagined as their unique signatures in THz spectrum. Predetermined locations and the amplitudes of these absorption lines is used to identify unknown molecules through spectroscopic techniques [14]. Having longer wavelengths than optical waves reveals another important advantage, reduced scattering. As a result, THz waves has an increased penetration into numerous dry materials such as textile, paper and wood which are normally opaque at wavelengths in the optical region of the electromagnetic spectrum. Moreover, having shorter wavelengths than microwave region provides imaging abilities with higher resolution [15].

In spite of these advantages, terahertz radiation has a certain disadvantage which limits its areas of application and also closely related to the main research problem of this thesis. It is the high THz absorption caused by water. This high absorbance prevents THz waves to penetrate into any material containing water and therefore reduces its usefulness in spectroscopy and imaging for such materials. In addition, due to the water vapor in atmosphere, constructing free space THz communication systems becomes impractical [10].

On the other hand, being absorbed by water prevents any harm done by THz radiation to biological structures. Also the energy THz photons possess is low enough to not being able to remove electrons from biological tissues or other materials. That is, THz radiation does not cause any photoionization and it is completely safe for humans and other living beings [16].

Methods of obtaining and detecting THz radiation vary greatly. Mainly there two groups which are called pulsed and continuous wave (CW) sources. The classification stems from the frequencies at which sources work and their type of emission. In addition, their manufacturing methods also differ for CW and pulsed sources. Pulsed sources are mostly based on optical techniques whereas CW sources rely on electronics [17]. As stated previously, pulsed and CW sources vary according to their operation frequencies. Pulsed sources provide a broadband emission in pulses in picosecond (ps) range. For CW sources, on the other hand, emission bandwidth is narrow and as the name suggests it is continuous.

The main application areas of THz frequency are imaging and spectroscopy. For systems in time domain such as the one which is proposed in this thesis, pulsed sources are preferred since they offer a temporal resolution in picosecond (ps) scale and provide a terahertz range of frequencies [18].

1.1 TERAHERTZ GENERATION METHODS

Similar to many other frequencies which lie under the blackbody power spectrum curve as shown in Figure 1.2, according to Wien's law, at temperatures starting from 1.71 Kelvins which corresponds to a peak frequency of 100.5 GHz, THz generation

can be achieved through blackbody radiation from anything. Therefore, theoretically, any object can be transformed into a THz emitter [19][20].

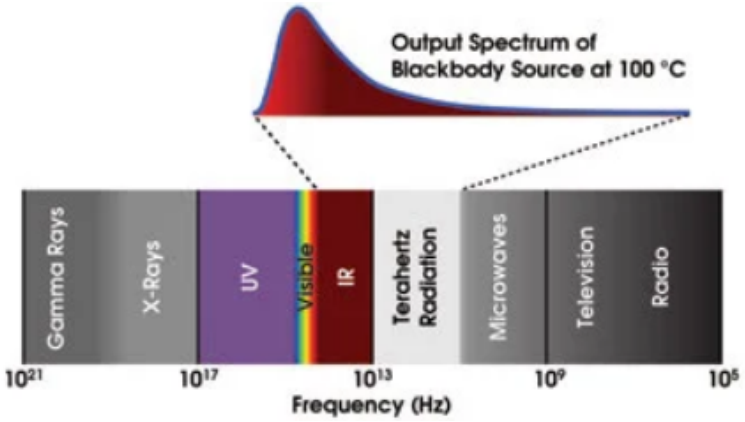

Figure 1.2: Blackbody radiation power spectrum curve and achievable frequencies. [2].

However, at terahertz frequencies, emission is too weak to be utilized in experimental systems. Therefore, in order to achieve enough emission power, different types of THz sources which are based either photoconductive emission, electro-optical rectification or surface emission have been manufactured over the years and they have been most commonly used in terahertz generation methods [2].

In surface emission method, semiconductors (SC) are used according to their energy band gap. The generation of the terahertz radiation strictly depends on the width of this gap and the carrier concentration. After being excited by an ultrafast laser, a spatial separation of an electron-hole pair near the material surface results in a charge dipole formation which in turn generates THz radiation in materials with a narrow band gaps such as InSb and InAs. For semiconductor materials with wider band gaps, the generation occurs as a result of photo-excited carrier acceleration. InP and GaAs can be given as an example for such materials [21] [22].

Crystals with birefringent properties such as ZnTe, GaSe, GaP, $LiNbO_3$ are used in optical rectification method as the medium of interaction for ultrafast laser pulses. Normally, when a light wave is sent through one of the aforementioned materials which have nonlinearity in order of χ^2, an electric field and frequency dependent nonlinear polarization with an average value different than zero is generated [23].

Usually, this nonlinear polarization does not have any considerable effect when the optical power of the incident light is constant or varies slowly in time. On the other hand, if the incident light becomes pulses generated by an ultrafast laser, the nonlinear polarization shows rapid oscillations in its strength. This very fast changes then results in a EM pulse radiation with a broad range of frequency varying from zero to a maximum value which is determined by the inverse of the ultrafast pulse duration. With suitable pulse widths, THz generation beyond 30 THz can be achieved [24].

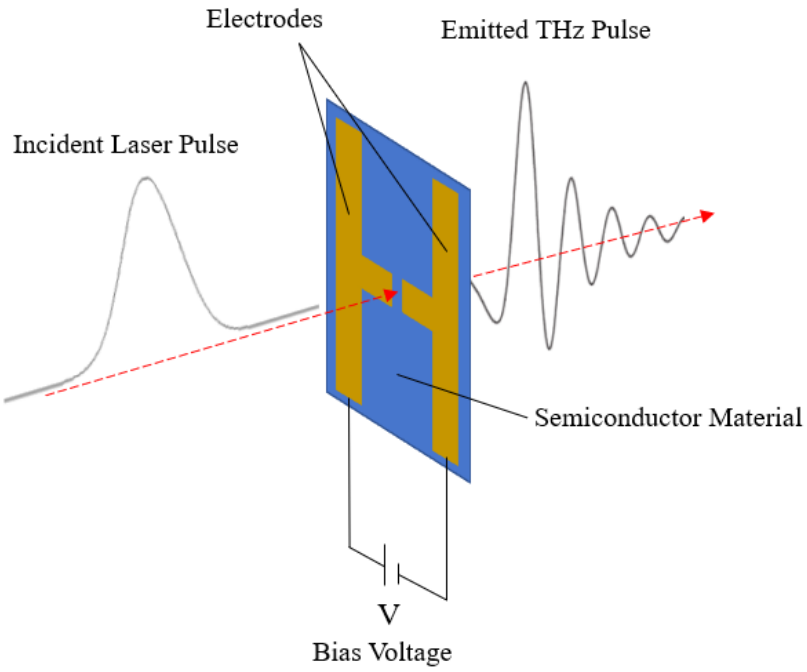

Figure 1.3: Schematic of THz generation with PCAs.

The third method, photoconductive emission, is mostly used in antenna structures called photoconductive antennas (PCAs). In PCAs, a semiconductor chip generates THz emission after photo-excitation caused by an ultrafast laser source [25]. A high resistive semiconductor chip is connected to a pair of electrodes having a few microns wide gap between each other. A laser pulse generated by an ultrafast laser with photon energy higher than the energy gap of the semiconductor is directly focused onto this gap. Having more energy than the energy gap creates free electrons in the conduction band and holes in the valence band after photon absorption. A DC bias voltage applied to the electrodes accelerates excited carriers because of the generated electric field. In other words, a swift change in the potential creates an oscillating transient current.

Finally, as a result of this transient current, emission of the THz waves occurs [26]. Figure 1.3 is given as an illustration of photoconductive emission process.

1.2 TERAHERTZ DETECTION METHODS

Terahertz detection methods are mostly based on PCAs and electro-optic (EO) sampling [27]. The principle which lies behind the electro-optic sampling is the Pockels effect. It is the change in the birefringence or refractive index of an EO crystal which is used as an optical medium. The change in birefringence occurs as a result of an applied electric field. In order to detect the incident optical signal, changes in the birefringence due to the electric field of the signal is measured. The Pockels effect is also a second order nonlinear process similar to optical rectification method. Materials such as EO polymers, organic crystals, ZnTe, GaAs are usually chosen as the optical medium.

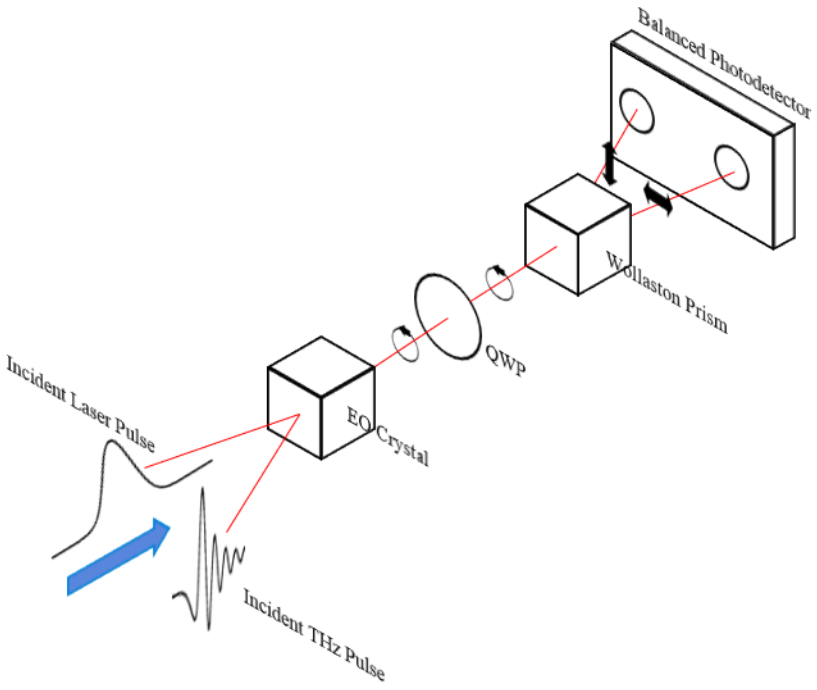

Figure 1.4: Schematic of electro-optic THz detection process.

The interaction of the ultrafast laser beam with the incident THz pulse inside the EO crystal changes the linear polarization state of the laser pulse into elliptical. After the EO medium, a quarterwave plate (QWP) is placed for polarization control. Then a

Wollaston prism separates the perpendicular components of the elliptical polarization into two parts. Finally, a balanced photodetector measures the differences in intensity of these two perpendicular parts of polarization. In the absence of an incident THz beam however, the linear polarization state of the ultrafast laser pulse transforms into circular. That is, separated perpendicular parts of the circular polarization have the same intensity. In this case, a balanced photodetector cannot generate a signal due to intensity difference. This means that the existence of a signal depends on the existence of a THz pulse inside the medium as it changes the polarization state of the laser pulse. As mentioned above, this change in polarization is proportional to the electric field of the incident THz pulse due to the Pockels effect. Therefore, the produced signal will be proportional to the electric field of the incident THz pulse. An illustration of this process is given in Figure 1.4.

Terahertz detection with PCAs is not much different than THz generation. In terms of structure, both antenna types are the same. However, in detection antennas, instead of a voltage source, electrodes are connected to an ammeter as shown in Figure 1.5.

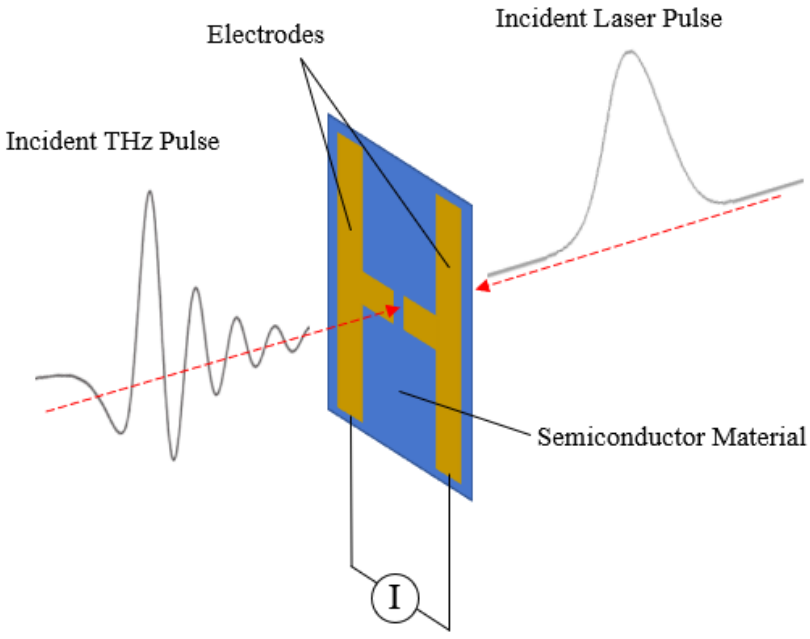

Figure 1.5: Schematic of THz detection with PCAs.

The physical process behind the detection does not differ either. In fact, it is the reverse of generation process. The ultrafast laser pulse which is focused onto the antenna gap again generates electron-hole pairs inside the semiconductor material.

When a THz pulse falls onto the antenna, generated carriers are again separated but this time the electric field is due to the incident THz beam. The existence of an electric field accelerates carries and as a result of this acceleration, a current with magnitude directly proportional to the electric field of THz wave is generated. If there is not an incident terahertz beam, current generation does not occur even if the carrier pairs are generated. The intensity of the incident terahertz beam is determined by measuring generated current [28].

1.3 TERAHERTZ TIME DOMAIN SPECTROSCOPY

The Fourier transform infrared (FTIR) spectroscopy has opened a new door for spectroscopy research since the middle of 20th century. The far-infrared region has gained and is still gaining more and more interest each day [29]. In spite of all advantages FTIR provides, when it comes to detecting phase changes and obtaining amplitude information together to determine the optical properties of materials, FTIR falls behind the terahertz time domain spectroscopy (THz-TDS) [30].

Terahzertz time domain spectroscopy (THz-TDS), teraherz emission spectroscopy (TES) and time-resolved terahertz spectroscopy (TRTS) are three main spectroscopy methods in terahertz region of electromagnetic spectrum [31].

THz-TDS technique, the method utilized in this thesis, is frequently preferred out of others mentioned previously for optical characterization of materials at terahertz frequencies. Providing a wide range of frequencies with a coherent detection is just one of the reasons for its preference [14]. In a THz-TDS system a laser beam generated by an ultrafast mode-locked laser source is divided into two for generation and detection of THz signal. By time sampling and recording the amplitude of the terahertz electric field, the entire THz wave is detected as a function of time. Two measurements, one with a sample and one without a sample, in time domain are compared after transferred to frequency domain and necessary information is obtained through signal analysis [32].

TRTS method, on the other hand, is used to probe dynamic properties of materials unlike THz-TDS which examines static properties. In terms of construction, THz-TDS

and TRTS systems are very similar. There are two beams to generate and detect THz signal. The only difference is the additional third laser beam used for photoexcitation. After excitation, changes in the materials induced by the third beam is observed.

Lastly in TES method, sample is used as the source of THz radiation. An amplified laser is utilized to send pulses to sample material in order to generate THz radiation. After achieving emission, the shape of the emitted THz wave and the amplitude of electric field is recorded.

1.4 TIME DOMAIN TERAHERTZ ATR SPECTROSCOPY

THz-TDS systems have been used to determine optical characteristics of a wide range of materials from liquids [33] [34] to semiconductors [35]. However, measuring polar liquids, especially water, has always been a challenging task due to the high absorbance they exhibit at terahertz frequencies. Inability to investigate water properly has also slowed down biological research in THz region due to the high amount of water contained in biological materials. In addition, measuring aqueous solutions were also a problem for the same reason. Therefore, new methods, especially based on reflection spectroscopy, have been considered in order to overcome this difficulty [36]. In 2004, a new method called attenuated total reflection (ATR) spectroscopy was proposed by Hirori et al. [37] in THz region and it has become one of the most prominent techniques in THz spectroscopy. In addition to its novelty, the THz ATR-TDS has been proved to be the most sensitive and effective method for optical characterization of liquids which show high absorption in the THz region of electromagnetic spectrum [38]. Since its first implementation, some of the studies with the THz ATR-TDS technique reported in literature include, investigation of heavy water by Yada et al. [39], monolayer cells by Shiraga et al. [40], water [41] by Nagai et al., measuring optical properties of porcine tissues including dermis, muscle and subcutaneous tissue by Sasaki et al. [42], determination of absorptive properties of explosive materials by Palka et al. [43].

A THz ATR-TDS system is constructed according to the basics of ATR geometry and terahertz spectroscopy. The main instrument utilized in the system is an evanescent

electric field which occurs as a result of total internal reflection (TIR) of THz waves. In order to achieve TIR, usually a Dove prism with a high refractive index and high transparency at THz frequencies is chosen. Germanium and high resistivity silicon are the most preferred materials for ATR prisms with their refractive indices of $\sim$3.42 and $\sim$4 respectively. However, materials with relatively higher refractive indices should be avoided as they cause increased Fresnel losses at the ATR interface [44].

Despite the broadened horizons by THz ATR-TDS technique in the area of terahertz spectroscopy, the method itself relies on many critical aspects which require immense attention for obtaining accurate results. The misalignment of the ATR prism [45], any changes in the incidence angle of THz waves [46], the efficiency of THz propagation in the system [44] are factors which affect the system stability in great measures even with small deviations. Therefore, properly constructing a THz ATR-TDS system requires more time and strenuous effort compared to common THz-TDS systems and due to the increased sensitivity to environmental effects and experimental errors which are usually negligible in other THz-TDS systems, rising the confidence level in acquired data and results is quite arduous.

In this thesis, a THz ATR-TDS system is presented. The system provides a solution for the problem of optical characterization of high absorptive materials and solutions include such materials at THz frequencies. Chapter 2 explains the theoretical background of the THz ATR-TDS technique in detail with rigorous analysis and figures. In addition, some of the points mentioned here also explained again more comprehensively. In Chapter 3, technical and experimental aspects of the constructed THz ATR-TDS system and the important points taken into account during the construction process are given. Chapter 4 shows the results of the experiments. Lastly, the overall discussion of the results and a summary of the study is given in Chapter 5.

CHAPTER 2

TIME DOMAIN TERAHERTZ ATR SPECTROSCOPY

THz ATR time domain spectroscopy method is based on the total internal reflection (TIR) principle. An evanescent THz wave created as a result of the internal reflection is utilized in order to optically characterize samples. This chapter explains the fundamentals of constructing such a time domain spectroscopy system and the theory behind it. Then it discusses the methods of sample measurements and constructs a mathematical basis for data analysis.

2.1 BASICS OF TERAHERTZ TIME DOMAIN SPECTROSCOPY

In general, most of the time domain THz spectroscopy systems are designed to use a pump probe beam. It is a very common way to construct a time domain spectroscopy system [47]. The whole operation can be summarized as follows the generation of a pump and probe beams from a laser source, introducing a time delay between them, and obtain sampling in time domain by using the probe beam as a result of the introduced time delay. The more detailed explanation of the process is given below.

A pulse coming from the ultrafast laser source is divided into two different arms which are called pump beam and probe beam by using a wavelength and percentage suitable beamsplitter. In most systems, this initial division is done by using 50:50 beam splitters which divide the incoming pulse almost equally into two in terms of optical power but depending on the design, different percentages are also used. Since the two beams are generated by the same laser source, they are mutually coherent.

The pump beam is directly sent to the THz generator. The probe beam on the other hand is first sent to take an additional path called delay line which is usually constructed by using a motorized stage and a retroreflector to achieve time delay. Then it is sent to the THz detector to sample the received THz signal. As the stage moves, it gradually changes the time probe beam reaches the detector and therefore with each step, a different portion of the generated THz beam is scanned by the probe beam and detected THz by the detector. A constant movement along the delay line results in the complete sampling of the THz pulse generated by the emitter in time domain with respect to the time delay. That is, the THz beam is captured as a function of time.

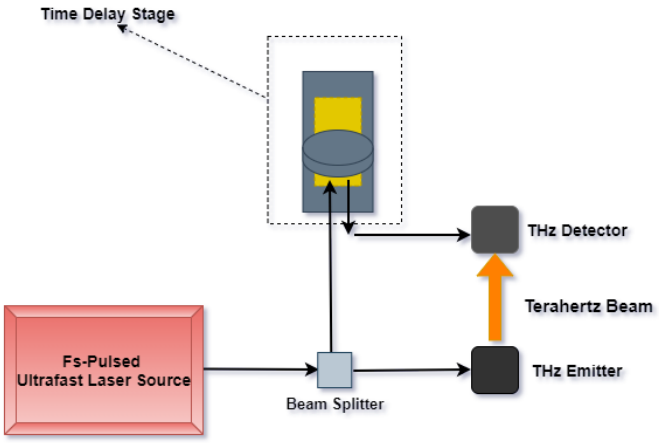

Figure 2.1: A Simplified illustration of THz Time Domain Spectroscopy Systems

Apart from the laser source and the delay stage, in a THz time domain spectroscopy (TDS) system, if a PCA is used for the generation of THz signal, a function generator, which supplies a bias determined according to the antenna specifications, is used to supply an electric field to accelerate photocarriers generated by the pump beam falling on the PCA chip.

On the detection side, usually a lock-in amplifier is added to the setup for the signal measurement purposes. The lock-in is also modulated by the same function generator to capture the signal at the set frequency. Inside a lock-in amplifier, there is a phase sensitive detector circuit which operates by taking the modulation signal as a reference and comparing the frequency and phase of the incoming signal from the system to it. The parts of the signal reaching to the lock-in amplifier which have the same phase and frequency as the reference signal is captured and boosted. As a result, in

addition to measuring the signal, an increased signal to noise ratio is achieved due to the background noise suppression.

Standard THz-TDS systems utilize broadband sources. They offer a good SNR ratio below 3 THz [48], a temporal resolution in ps scale and the measurement the electric field of THz signal. This in turn, since the electric field carries the information about both phase and amplitude, allows the determination of refractive index and absorption coefficient of the sample.

2.2 TIME DOMAIN TERAHERTZ ATR SPECTROSCOPY PRINCIPLES

A THz ATR-TDS system is essentially no different than other THz time domain spectroscopy systems for the fundamental points explained in the previous section as it is, in the end, nothing but another method of a spectroscopy in time domain. The experimental setups are mostly the same but there are also numerous important aspects of a THz ATR system which require a different approach in terms of both theory and experiment.

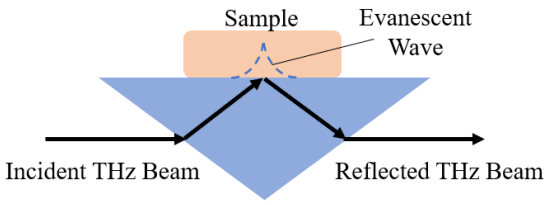

Figure 2.2: ATR Prism

The figure above is a simplified representation of maybe the most important part of a THz ATR-TDS system. It is where the total internal reflection and sample-THz interaction occurs. Incident THz pulse generated by the emitter is focused through a Si prism which is highly transparent to THz frequency, to be reflected at its base according to the total internal reflection (TIR) principle. An evanescent wave, that is the electromagnetic field accompanied by the reflected THz beam which passes through the reflection interface up to a certain length, interacts with the sample placed on the outside of the base of the prism as it propagates along the reflection interface

[41]. Later, the information about this sample-evanescent wave interaction which is in the form of an attenuation in reflection and proven to be linearly related to the absorption coefficient of the samples, is carried to the detector by the reflected THz pulse and recorded [49].

Before starting to construct a THz ATR-TDS system, it is extremely important to understand the two main pillars of the theory. The total internal reflection principle of electromagnetic waves at a boundary and the penetration depth which is the distance evanescent wave travels after passing through the reflection interface. The design of the whole system, sample measurements and data analysis are done according to these two concepts. Therefore, in the following sections, both will be explained in detail and the derivations of the essential mathematical expressions will be provided.

2.2.1 TOTAL INTERNAL REFLECTION

Figure 2.3 below is an illustration of a light beam that is propagates in a medium with refractive index n_1 and moves towards a medium with refractive index of n_2.

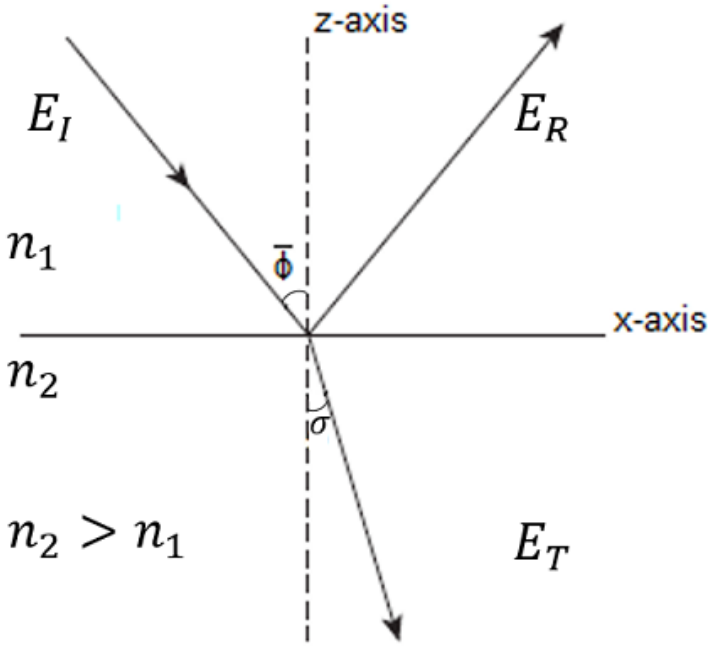

Figure 2.3: Incident, transmitted, and reflected light at the interface between two media with refractive indices n_1 and n_2 where $n_2 > n_1$.

It can be seen that at the boundary, a portion of the incident light E_I is reflected as E_R and remaining portion is transmitted to the other medium as E_T. Throughout this thesis, the same notation will be followed for consistency.

Maxwell's equations for electromagnetic waves in a linear and homogeneous medium with no free current or free charge are given below.

$$\nabla \cdot E = 0 \tag{2.1}$$

$$\nabla \cdot B = 0 \tag{2.2}$$

$$\nabla \times E = -\frac{\partial B}{\partial t} \tag{2.3}$$

$$\nabla \times B = \varepsilon\mu\frac{\partial E}{\partial t} \tag{2.4}$$

A few steps of trivial mathematical manipulations applied to Maxwell's equations result in the wave equations for E and B in three dimensions.

$$\nabla^2 E = \mu\varepsilon\frac{\partial^2 E}{\partial t^2} \tag{2.5}$$

$$\nabla^2 B = \mu\varepsilon\frac{\partial^2 B}{\partial t^2} \tag{2.6}$$

The solutions of these two differential equations give the wave functions for electrical and magnetic field.

$$E(r,t) = E_0 e^{i(k\cdot r-\omega t)} \tag{2.7}$$

$$B(r,t) = B_0 e^{i(k\cdot r-\omega t)} \tag{2.8}$$

Eqs. 2.7 and 2.8 can be related to each other throughout a constraint set by Maxwell's equations which implies perpendicularity of these two wave functions.

$$B(r,t) = \frac{1}{v}\hat{k} \times \hat{E} \tag{2.9}$$

Then Eqs. 2.7 and 2.8 can be rewritten as

$$E(r,t) = E_0 e^{i(k\cdot r-\omega t)}\hat{n} \tag{2.10}$$

$$B(r,t) = \frac{1}{v}E_0 e^{i(k\cdot r-\omega t)}(\hat{k} \times \hat{n}) \tag{2.11}$$

Where

$$v = \frac{1}{\sqrt{\varepsilon\mu}} = \frac{c}{n} \tag{2.12}$$

$$n \equiv \sqrt{\frac{\varepsilon\mu}{\varepsilon_0\mu_0}} \tag{2.13}$$

At a boundary between two different media, electric and magnetic fields obey a set of boundary conditions which can be derived from Maxwell's equations.

$$\varepsilon_1 {E_1}^{\perp} = \varepsilon_2 {E_2}^{\perp} \tag{2.14}$$

$${B_1}^{\perp} = {B_2}^{\perp} \tag{2.15}$$

$${E_1}^{\parallel} = {E_2}^{\parallel} \tag{2.16}$$

$$\frac{1}{\mu_1}{B_1}^{\parallel} = \frac{1}{\mu_2}{B_2}^{\parallel} \tag{2.17}$$

These conditions indicate that at a boundary, the tangential components of the electric field are continuous (Eq. 2.7) whereas the normal components have a jump depending on the dielectric constants of the two media (Eq. 2.5) [50]. For the magnetic field, on the other hand, tangential components have a jump which depends on the magnetic permeability of the media (Eq. 2.8) and the normal components are continuous (Eq. 2.6).

Eq. 2.9 and the assumption of $\mu \cong \mu_0$ [51][50] for the two media reduces Eq. 2.13 to $n \cong \sqrt{\varepsilon_r}$. In addition, the boundary conditions given previously now can be rearranged as follows according to the incident, reflected and transmitted waves shown in Figure 2.3

$$\varepsilon_1 \left(\boldsymbol{E}_{\mathrm{I}}^{\perp} + \boldsymbol{E}_R^{\perp}\right) = \varepsilon_2 \boldsymbol{E}_T^{\perp} \tag{2.18}$$

$$n_1 \boldsymbol{k}_{\mathrm{I}} \times \boldsymbol{E}_{\mathrm{I}}^{\perp} + n_1 \boldsymbol{k}_R \times \boldsymbol{E}_R^{\perp} = n_2 \boldsymbol{k}_T \times \boldsymbol{E}_T^{\perp} \tag{2.19}$$

$$\left(\boldsymbol{E}_{\mathrm{I}}^{\parallel} + \boldsymbol{E}_R^{\parallel}\right) = \boldsymbol{E}_T^{\parallel} \tag{2.20}$$

$$n_1 \boldsymbol{k}_{\mathrm{I}} \times \boldsymbol{E}_{\mathrm{I}}^{\parallel} + n_1 \boldsymbol{k}_R \times \boldsymbol{E}_R^{\parallel} = n_2 \boldsymbol{k}_T \times \boldsymbol{E}_T^{\parallel} \tag{2.21}$$

The polarization of the incident wave plays a very important role in further calculations. Therefore, it is best to analyze both s-polarized and p-polarized waves separately. For s-polarization (electric field is perpendicular to the plane of incidence), Eqs. 2.18 and 2.19 are just identity and Snell's Law respectively. The other two equations become

$$E_I + E_R = E_T \tag{2.22}$$

$$n_1 (E_I - E_R) \cos\overline{\phi} = n_2 E_T cos\sigma \tag{2.23}$$

Then by introducing reflection and transmission coefficients r^s and t^s, Eqs. 2.22 and 2.33 can be solved as

$$r^s = \frac{E_R}{E_I} = \frac{n_1 \cos\overline{\phi} - \sqrt{n_2^2 - n_1^2 \sin^2\overline{\phi}}}{n_1 \cos\overline{\phi} + \sqrt{n_2^2 - n_1^2 \sin^2\overline{\phi}}} \tag{2.24}$$

$$t^s = \frac{E_T}{E_I} = \frac{2n_1 \cos\overline{\phi}}{n_1 \cos\overline{\phi} + \sqrt{n_2^2 - n_1^2 \sin^2\overline{\phi}}} \tag{2.25}$$

The same procedure is repeated for p-polarization (electric field is parallel to the plane of incidence).

$$(E_I - E_R)\cos\overline{\phi} = E_T \cos\sigma \tag{2.26}$$

$$n_1 (E_I + E_R) = n_2 E_T \tag{2.27}$$

After the introducing r^p and t^p again for p-polarization,

$$r^p = \frac{E_R}{E_I} = -\frac{n_2^2 \cos\overline{\phi} - n_1\sqrt{n_2^2 - n_1^2 \sin^2\overline{\phi}}}{n_2^2 \cos\overline{\phi} + n_1\sqrt{n_2^2 - n_1^2 \sin^2\overline{\phi}}} \tag{2.28}$$

$$t^p = \frac{E_T}{E_I} = \frac{2n_1 n_2 \cos\overline{\phi}}{n_2^2 \cos\overline{\phi} + n_1\sqrt{n_2^2 - n_1^2 \sin^2\overline{\phi}}} \tag{2.29}$$

Eqs. 2.24, 2.25, 2.28 and 2.29 are called Fresnel coefficients. They are used to calculate the magnitude of the reflected and transmitted electric fields of the waves at a boundary with respect to the electric field of the incident wave. Superscripts s and p identify the direction of polarization.

After deriving necessary equations to calculate the reflection and transmission for a wave incident on an interface between two media, it is now easier to consider a case where light is sent from an optically denser medium to an optically rarer medium as shown in Figure 2.4 on the next page.

According to Snell's Law, for every incidence angle $\overline{\phi}$ there is an angle of refraction σ that is strictly dependent on the refractive indices of two different media. In the case of incidence from a denser medium, when angle $\overline{\phi}$ approaches a certain value of $\overline{\phi}_m$, the refraction angle σ starts to approach $90°$.

$$n_2 \sin\overline{\phi} = n_1 \sin\sigma \tag{2.30}$$

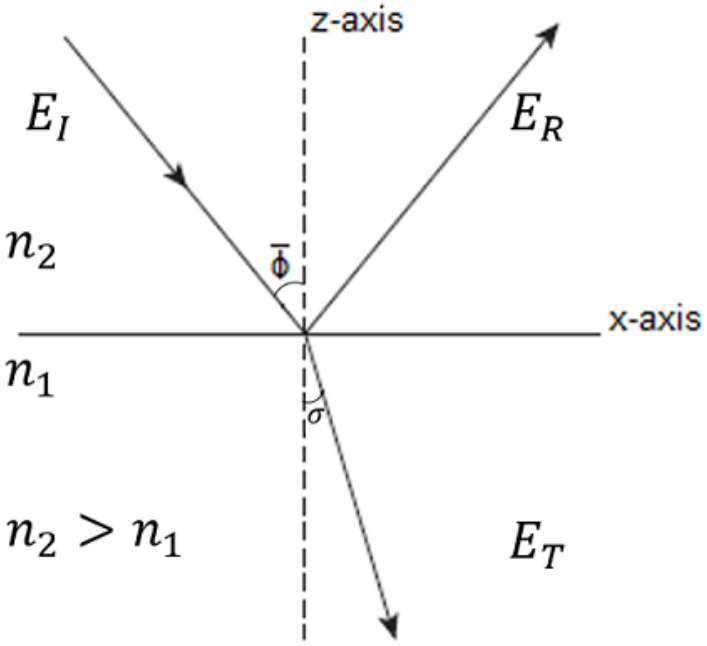

Figure 2.4: Incident, transmitted, and reflected light at the interface between two media with refractive indices n_1 and n_2 where $n_2 > n_1$.

Fresnel reflection coefficients of light for s and p polarization directions then become

$$r^s = \frac{E_R}{E_I} = \frac{n_2 \cos\overline{\phi} - \sqrt{n_1^2 - n_2^2 \sin^2\overline{\phi}}}{n_2 \cos\overline{\phi} + \sqrt{n_1^2 - n_2^2 \sin^2\overline{\phi}}} \tag{2.31}$$

$$r^p = \frac{E_R}{E_I} = -\frac{n_1^2 \cos\overline{\phi} - n_2\sqrt{n_1^2 - n_2^2 \sin^2\overline{\phi}}}{n_1^2 \cos\overline{\phi} + n_2\sqrt{n_1^2 - n_2^2 \sin^2\overline{\phi}}} \tag{2.32}$$

There is no physical constraint that prevents $\overline{\phi}$ to take values bigger than $\overline{\phi}_m$ but refraction angle σ cannot go beyond $90°$. As the incidence angle exceeds $\overline{\phi}_m$, refraction angle should get values that give $sin\sigma > 1$ which is not possible. As a result, refracted wave can no longer exist. It is obvious that Eq. 2.31 and 2.32 are given in terms of incidence angle. This makes obtaining reflection coefficients possible even when there is no refraction. There is, however, one important issue. When $\overline{\phi}$ goes beyond $\overline{\phi}_m$, the expression in square root becomes negative. This results in a complex Fresnel reflection coefficient in the given form.

$$r = \frac{A - iB}{A + iB} \tag{2.33}$$

The reflectance R then becomes

$$R = |r^2| = \frac{A^2 + B^2}{A^2 + B^2} = 1 \tag{2.34}$$

Eq. 2.34 is true for both s and p polarizations. It basically states that when the angle of incidence $\overline{\phi}$ goes further than the critical angle $\overline{\phi}_m$, the angle which makes the expression in the square root in Fresnel reflection coefficient formula zero, the reflection of the incoming wave at the interface between the two media becomes total. Figure 2.5 shows the reflectance values of p and s polarizations in terms of incidence angle. The $\overline{\phi}_m$ value after which the reflection becomes total can be identified.

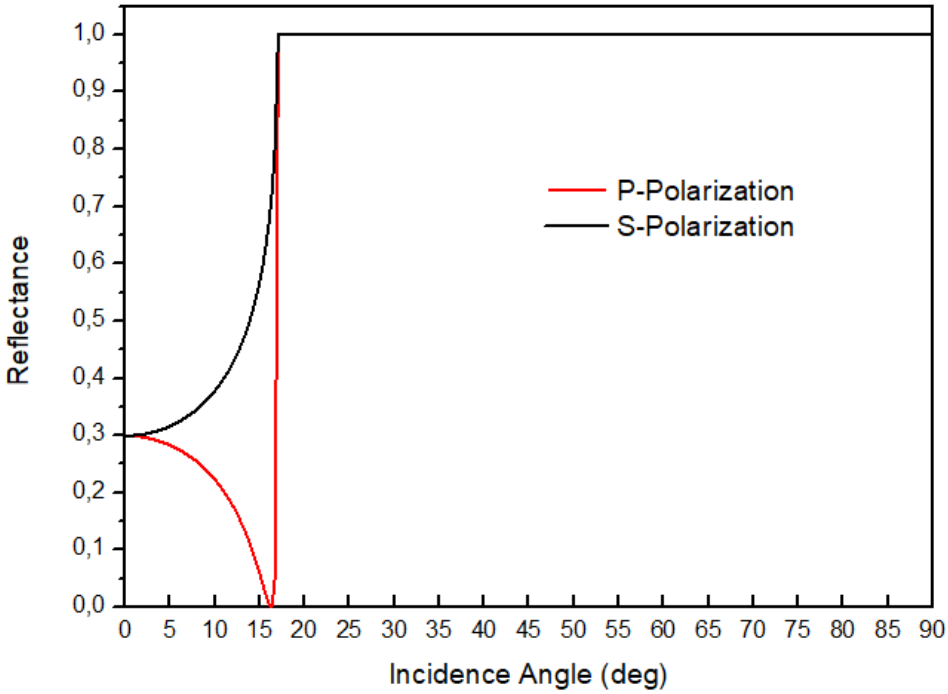

Figure 2.5: The reflectance of the light incident from a denser medium in terms of incidence angle calculated using MATLAB where $n_2 = 3.42$ and $n_1 = 1$.

The definition of critical angle makes it easier to find its value by using Snell's Law. In order to be consistent with other scientific sources, after this point the critical angle will be denoted as $\overline{\phi}_C$ instead of $\overline{\phi}_m$.

$$\overline{\phi}_C = \sin^{-1}\left(\frac{n_1}{n_2}\right) \tag{2.35}$$

Eq. 2.33 shows that the Fresnel reflection coefficient for total internal reflection is a complex value. It is a common knowledge that any complex value which is in the

form of $a + ib$ can be rewritten by using Euler's formula. Therefore, the Fresnel coefficient too can be written as

$$r = e^{i\kappa} \tag{2.36}$$

Where κ is a real value and it shows that a constant phase shift added to the reflected wave as a result of reflection. It is important to note that this phase shift is the same for everywhere on the boundary between the two media and obviously different for s and p polarizations. The value of κ can be calculated using Eq. 2.33 and 2.26.

$$\kappa = \arctan \frac{2AB}{A^2 + B^2} \tag{2.37}$$

In Figure 2.6, the plot shows the phase shift κ due to total internal reflection for s and p polarizations in terms of incidence angle.

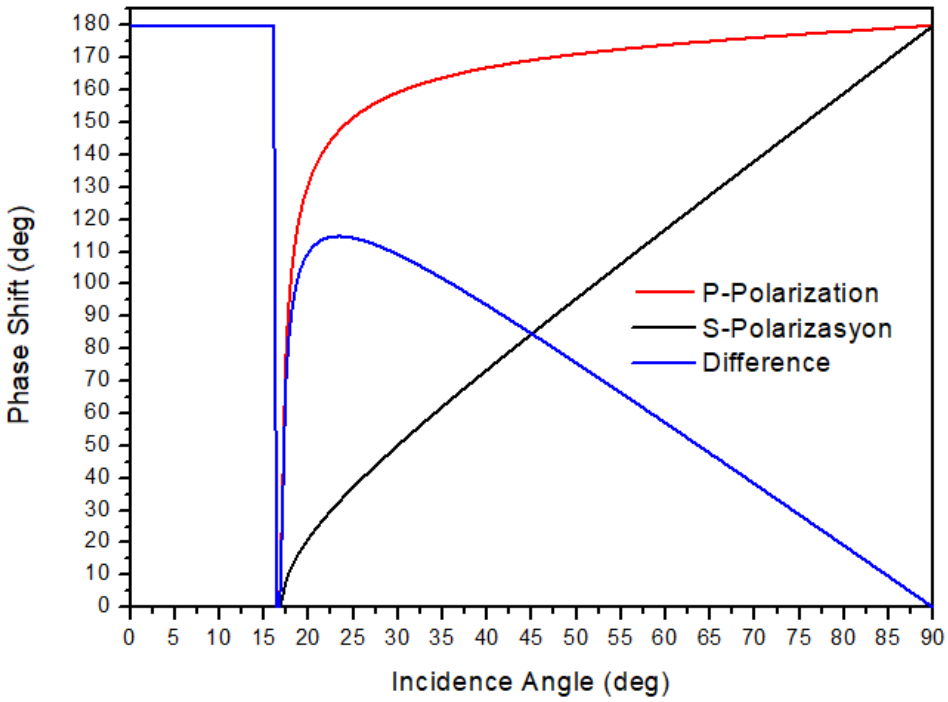

Figure 2.6: The phase shift due to total internal reflection for p and s polarizations calculated using MATLAB where $n_2 = 3.42$ and $n_1 = 1$.

2.2.2 PENETRATION DEPTH

It is explained in section 2.2 that when a THz beam is incident on a surface at which TIR occurs, an electromagnetic field penetrates to the other side of the interface and it decays exponentially as it propagates up to a certain distance. This decay of the evanescent wave is expressed as

$$e^{-r\alpha} \tag{2.38}$$

Where α is called the decay constant and it is strongly dependent on the refractive index value of optically rarer medium n_1 [52].

According to Figure 2.4, equations of reflected and transmitted waves are of the following form

$$\mathbf{E}_R(r,t) = E_R e^{i(k_t \cdot r - \omega t)} \tag{2.39}$$

$$\mathbf{E}_T(r,t) = E_T e^{i(k_r \cdot r - \omega t)} \tag{2.40}$$

If the exponent of the exponential part of transmitted wave equation is investigated closely, it is obvious that there exists a scalar product of wave and point of reference vectors. Taking the plane of incidence as xz plane and the normal to the interface as the z-axis in Figure 2.4, the aforementioned scalar product is then calculated as follows.

$$\frac{\omega}{k_t} = \frac{c}{n_1} \tag{2.41}$$

$$k_t = \frac{n_1 \omega}{c} \tag{2.42}$$

$$k_t = n_1 k_0 \tag{2.43}$$

Where $k_0 = \omega/c$ is the wavenumber in a vacuum and n_1 is the refractive index of the rarer medium. The wave vector in Eq. 2.40 now can be expanded as

$$k_t = n_1 k_0 (z cos\sigma + x sin\sigma) \tag{2.44}$$

After applying Snell's law to the x component, the wave vector becomes

$$k_t = k_0 (z n_1 cos\sigma + x n_2 sin\overline{\phi}) \tag{2.45}$$

The scalar product in the wave equation is now equal to

$$k_t \cdot r = k_0 (n_2 x \sin\overline{\phi} + n_1 z \cos\sigma) \tag{2.46}$$

Which allows Eq. 2.40 to take the form given below

$$\mathbf{E}_T(r,t) = E_T e^{i(n_2 k_0 x \sin\overline{\phi} + n_1 k_0 z \cos\sigma - \omega t)} \tag{2.47}$$

Where σ is the angle of refraction. Since total internal reflection theory states that total reflection occurs at the interface, the refraction angle σ does not exist. This means it is a necessary to write σ in terms of the incidence angle $\overline{\phi}$.

$$\cos\sigma = \sqrt{1-\sin^2\sigma} = \sqrt{1-(n_2/n_1)^2\sin^2\overline{\phi}} \tag{2.48}$$

The final form of the scalar product for the transmitted wave is then becomes

$$k_0(n_2 x sin\overline{\phi} + n_1 z cos\sigma) = k_0\left(n_2 x sin\overline{\phi} + z n_1\sqrt{1-(n_2/n_1)^2\sin^2\overline{\phi}}\right) \tag{2.49}$$

Inserting Eq. 2.52 into the transmitted wave equation (Eq. 2.50) results in

$$\mathbf{E}_T(\mathbf{r},t) = \mathbf{E}_T e^{-i\omega t} e^{in_2 k_0 x sin\overline{\phi}} e^{-k_0 z\sqrt{n_2^2 sin^2\overline{\phi} - n_1^2}} \tag{2.50}$$

Which can be abbreviated

$$\mathbf{E}_T(r,t) = \mathbf{E}_T e^{-\alpha z} e^{i(k\cdot x - \omega t)} \tag{2.51}$$

Where

$$\alpha = k_0 z\sqrt{n_2^2 sin^2\overline{\phi} - n_1^2} \tag{2.52}$$

The first exponential part of Eq. 2.53 describes the oscillatory nature of the wave. The second part explains its propagation along the reflection interface (x-axis) with $k_x = k_0 n_2 sin\overline{\phi}$. The last part represents the exponential decay of the evanescent wave which moves in the direction of the z-axis. Basically, it is what is left from the refracted wave as the angle of incidence $\overline{\phi}$ gets bigger than the critical angle. The amplitude is the largest at the interface and it gets damped as it moves further away from the interface. The distance at which the amplitude of the evanescent wave falls to $1/e$ of its maximum is called the penetration depth and it is denoted as d_p. Its value is equal to $d_p = 1/\alpha$.

$$d_p = \frac{1}{k_0\sqrt{n_2^2 sin^2\overline{\phi} - n_1^2}} = \frac{c}{2\pi\nu_0\sqrt{n_2^2 sin^2\overline{\phi} - n_1^2}} \tag{2.53}$$

Where ν_0 is the frequency of incident light in vacuum and $k_0 = 2\pi\nu_0/c$.

The plot on the next page shows different penetration depth values for different frequencies in terms of the incidence angle. It should be noted that the evanescent wave starts to penetrate into the other side of the interface as soon as total internal reflection occurs.

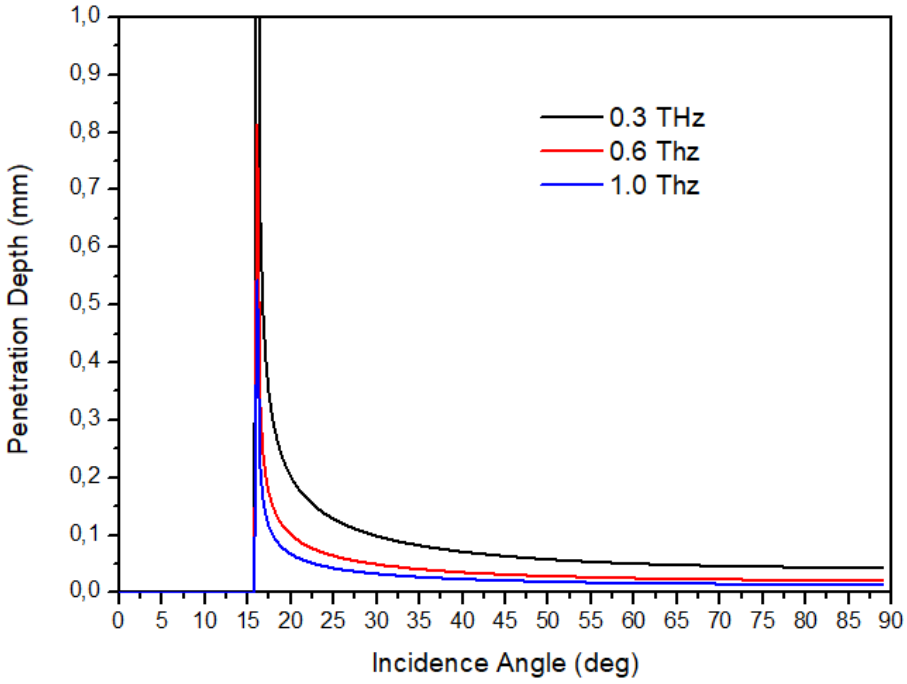

Figure 2.7: Penetration depth at 0.3, 0.6 and 1 THz in terms of incidence angle calculated using MATLAB where $n_2 = 3.42$ and $n_1 = 1$.

2.2.3 MEASUREMENTS AND DATA ANALYSIS

In previous sections, the theory behind the system has been explained in detail and points which require attention have been pointed out. In this section general principles which lie behind the sample measurements and the analysis of the recorded time domain data will be explained.

Refractive index and absorption coefficient determination are one of the simplest and fastest methods to classify materials. For THz transparent materials, there are several effective and proven methods [53], [54]. For non-transparent or high absorptive materials, ATR-TDS method is utilized.

Time domain analysis is based on mathematical comparison of reference and sample signals which are obtained by the system [55]. In a THz ATR-TDS system, a reference signal is measured without anything on top of the Si prism base. Samples, on the other hand, are measured by placing them where THz beam is focused and reflected as shown in Figure 2.8. The alignment of the sample with respect to the THz focal point is a critical factor in measurements. A simple misalignment can cause serious errors in optical characterization of samples [56].

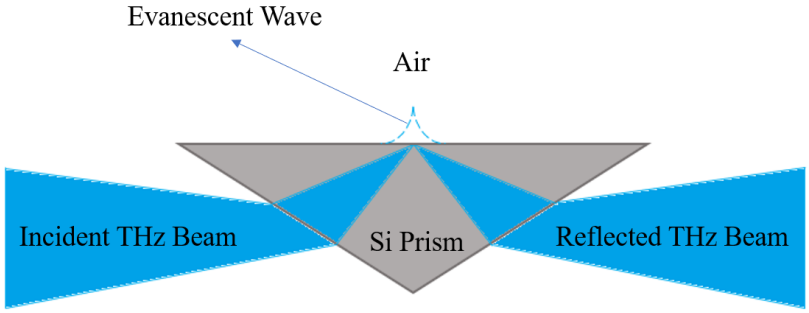

(a) Reference measurement.

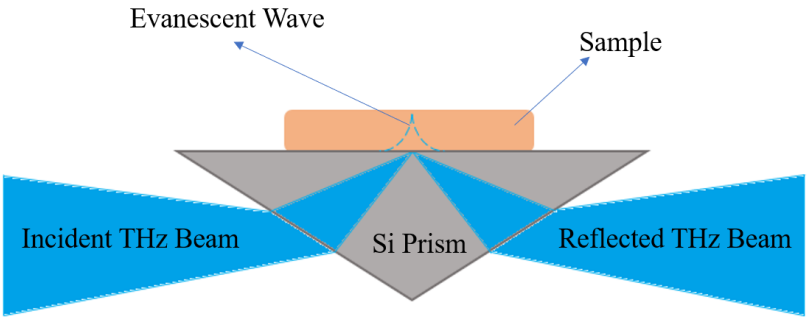

(b) Sample measurement.

Figure 2.8: An illustration of reference and sample measurements.

A reference measurement in time domain can be expressed as $E_{ref}(t)$. Similarly, the expression for sample measurements then becomes $E_{sample}(t)$. In order to determine optical properties of materials, these two time domain signals are transferred into frequency domain through Fourier transformation as follows.

$$E_{ref}(t) \overset{\text{FT}}{\rightarrow} \frac{1}{\sqrt{2\pi}} \int_{-\infty}^{\infty} E_{ref}(t) \mathrm{e}^{-\mathrm{i}\omega t} \, \mathrm{d}t = E_{ref}(\omega) \tag{2.54}$$

$$E_{sample}(t) \overset{\text{FT}}{\rightarrow} \frac{1}{\sqrt{2\pi}} \int_{-\infty}^{\infty} E_{sample}(t) \mathrm{e}^{-\mathrm{i}\omega t} \, \mathrm{d}t = E_{sample}(\omega) \tag{2.55}$$

The ratio of frequency domain data of reference and sample measurements is equal to the ratio of their Fresnel reflection coefficients.

$$\frac{E_{sample}(\omega)}{E_{ref}(\omega)} = \frac{r_{sample}}{r_{ref}} \tag{2.56}$$

In section 2.2.1, Fresnel coefficients for s and p polarization directions were derived. Although there are no strict constraints for choosing a polarization direction for the incident THz beam, it is proven that p polarization is less affected by secondary reflections and prism deflections than s polarization. These factors make p polarization more preferable for THz ATR-TDS systems [53]. After deciding which polarization direction to use for THz beams, Eq. 2.56 can be rewritten as

$$\frac{E_{sample}(\omega)}{E_{ref}(\omega)} = Re^{(i\kappa)} = \frac{r^p_{sample}}{r^p_{ref}} \tag{2.57}$$

$$r^p_{sample} = r^p_{ref} Re^{(i\kappa)} \tag{2.58}$$

Where R is the amplitude and κ is the phase of the spectral ratio of the reference and sample signals. Using Eq. 2.32, r^p_{ref} can be calculated after replacing n_1 with $n_{air} = 1$ and n_2 with $n_{prism} = 3.42$. This makes the right hand side of Eq. 2.58 a known value. Using Eq. 2.32 once again for r^p_{sample} after replacing n_2 with n_{prism} and n_1 with n_{sample} leads to the following expression

$$r^p_{sample} = -\frac{n^2_{sample}\cos\overline{\phi} - n_{prism}\sqrt{n^2_{sample} - n^2_{prism}\sin^2\overline{\phi}}}{n^2_{sample}\cos\overline{\phi} + n_{prism}\sqrt{n^2_{sample} - n^2_{prism}\sin^2\overline{\phi}}} \tag{2.59}$$

It is clear that Eq. 2.62 is a function of n_{sample} as it is the only unknown term. By applying some trivial mathematical manipulations, the expression above can be inverted as

$$n^2_{sample} = \epsilon_{sample} = \frac{X \pm \sqrt{X^2 - YX\sin^2 2\overline{\phi}}}{2Y\cos^2\overline{\phi}} \tag{2.60}$$

Where $Y = (r^p_{sample} - 1)^2$ and $X = (r^p_{sample} + 1)^2$. It should be noted that n^2_{sample} is a complex value and therefore $\hat{\epsilon}_{sample}$ too is a complex value.

$$n_{sample} = n'_{sample} + ik_{sample} \tag{2.61}$$

$$n^2_{sample} = \epsilon_{sample} = \epsilon'_{sample} + i\epsilon''_{sample} \tag{2.62}$$

Almost all typical materials have a positive ϵ'' and therefore in Eq. 2.63 solutions with $\epsilon''_{sample} > 0$ should be chosen in order to obey energy conservation[38]. Finally, the following expressions for the real and imaginary parts of the complex refractive index can be derived from Eqs. 2.64 and 2.65.

$$\epsilon'_{sample} = n'^2_{sample} - k^2_{sample} \tag{2.63}$$

$$\epsilon''_{sample} = 2n'_{sample}k_{sample} \tag{2.64}$$

CHAPTER 3

TIME DOMAIN TERAHERTZ ATR SPECTROSCOPY SYSTEM

In this chapter, a detailed description of the THz ATR-TDS system constructed for optical characterization of absorptive samples is given. The system layout with the laser source, optical components, electronic and mechanical devices is presented. In addition, important points taken into account during the construction of the system such as the optical path length, spot size and the focal point location of THz beams are also explained. Finally, data collection and analysis are described.

3.1 LASER SOURCE

The laser source of the system is a Toptica FFS.SYS. It is an ultrafast mode-locked Erbium (Er) doped fiber laser based on nonlinear polarization rotation.

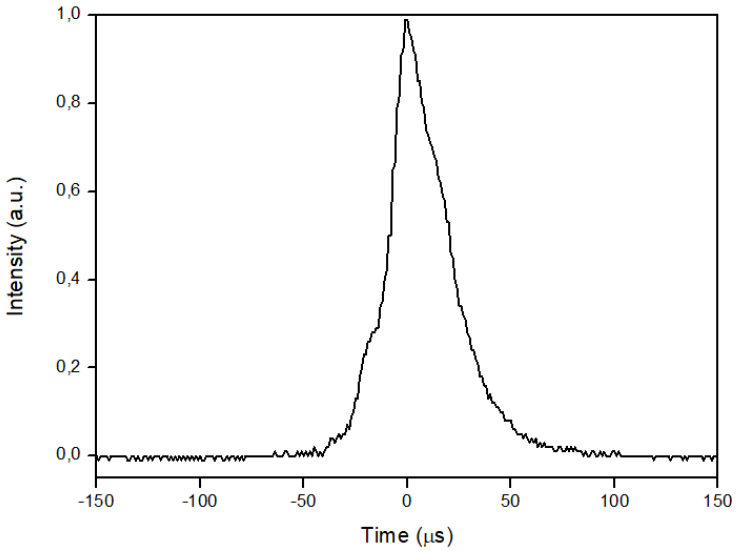

Figure 3.1: Autocorrelation measurement of the laser source.

Its average output power is 120 mW. The output is P polarized. It emits a center wavelength of 1550 nm at a 89 MHz repetition rate with a pulse width measured as 230 fs by using a Femtochrome FR-103 intensity autocorrelator at full width and half maximum (FWHM) with a Gaussian beam correction factor as shown in Figure 3.1.

3.2 SYSTEM LAYOUT

In Figure 3.2 below a schematic of the experimental system is given and the following is the component list.

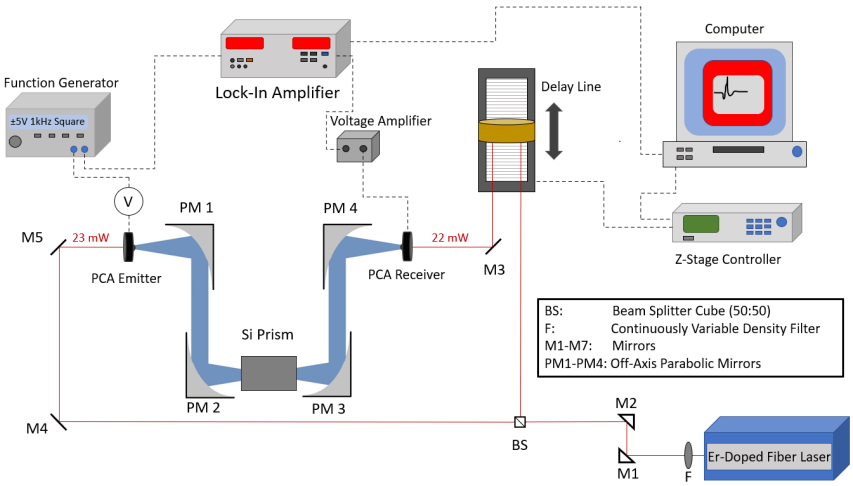

Figure 3.2: Schematic of the experimental THz ATR-TDS system.

1. Main Arm
   (a) Toptica FFS.SYS Erbium-doped mode locked fiber laser.
   (b) F: Round, continuously variable density filter
   (c) M1-M2: Flat mirrors.
   (d) 50:50 Beam splitter.
2. THz Generation Arm
   (a) M4-M5: Flat mirrors.
   (b) PCA: BATOP PCA-40-05-10-1550-h.
   (c) Function generator: RIGOL DG2041A.

3. Measurement Section

   (a) PM1-PM4: Off-Axis 90° Parabolic Mirror.

   (b) HRFZ-Si prism 54.85x21.74x35 mm. Base Angle: 103.2°

   (c) Prism holder.

4. Detection Arm

   (a) Delay Line: A gold corner retroreflector cube on a moveable stage.

   (b) M3: Flat Mirror.

   (c) PCA: BATOP PCA-100-05-10-1550-h .

5. Data Acqusition

   (a) Stage controller: Newport ESP301.

   (b) Lock-in amplifier: Stanford Research Systems SR850 DSP.

   (c) Computer.

Figure 3.3 and 3.4 show the experimental setup with labelled components.

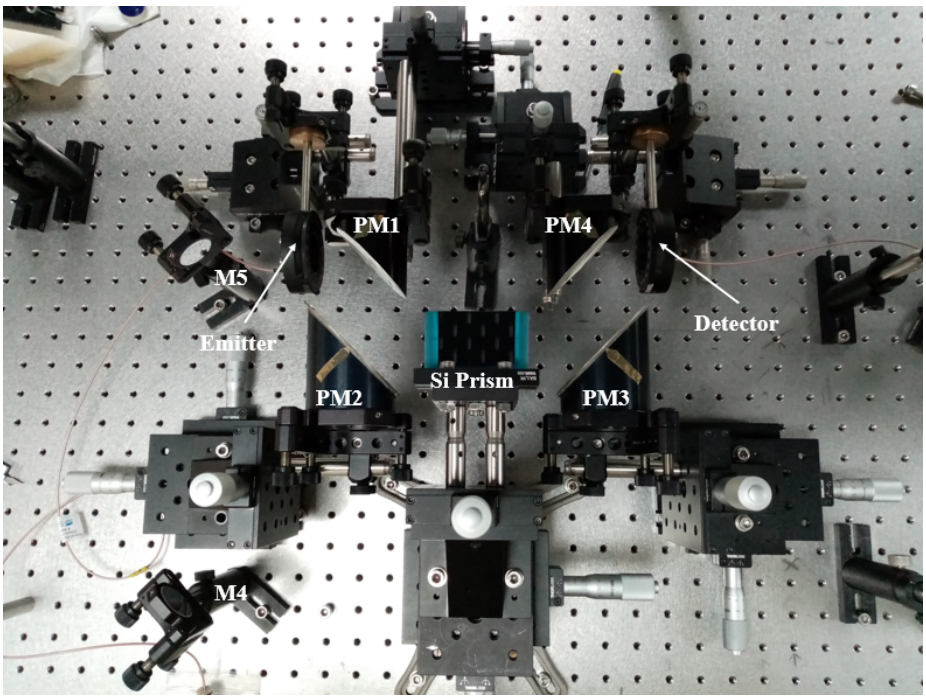

Figure 3.3: Constructed THz ATR-TDS System.

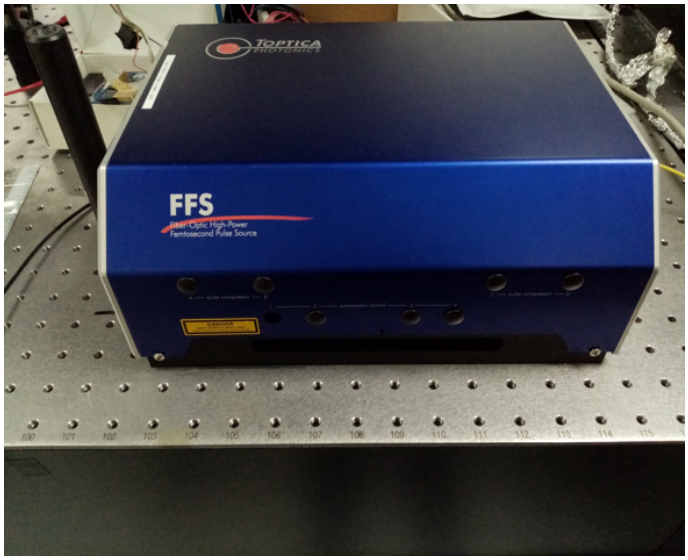

(a) Laser source.

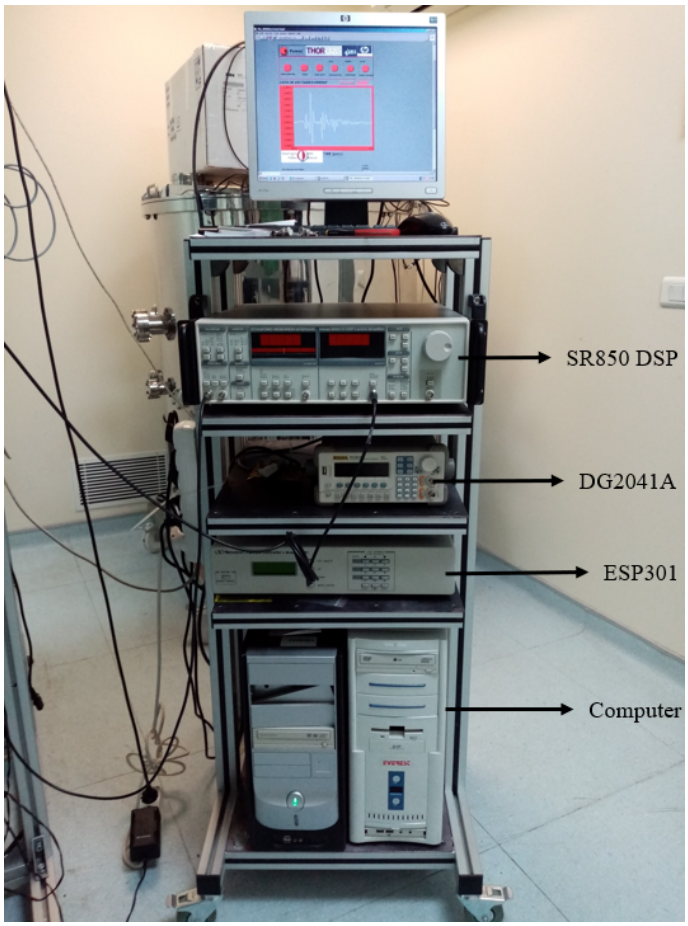

(b) System Rack.

Figure 3.4: Laser source and data acquisition devices.

The output of the laser source is sent through the adjustable filter (F) so that the light incident on THz antennas can be adjusted. Right after the filter a periscope mirror setup (M1,M2) raises the beam to 15 cm with respect to the optical table. Then, at the 50:50 beam splitter (BS) it is split into two equal parts in terms of optical power. These two parts of the laser output are used in the generation and detection arms. In generation arm, laser is first folded $90°$ by M4 and then it is folded $90°$ once again and sent to the gap of the THz generation antenna (PCA Emitter) by mirror M5. Laser power at the antenna is measured as 23 mW. The other portion of the output beam is sent to the gold retroreflector cube fixed on top of a movable stage (Delay Line) after the beam splitter. As the name suggests, it folds the laser beam $180°$ in total and sents it back to M3 at which laser light is directed at the THz detection antenna (PCA Receiver). The optical power of the light falling on the antenna is measured as 22 mW.

The THz generation antenna used in the system is a BATOP PCA-40-05-10-1550-h as previously stated. The structure of the antenna is given in Figure 3.5.

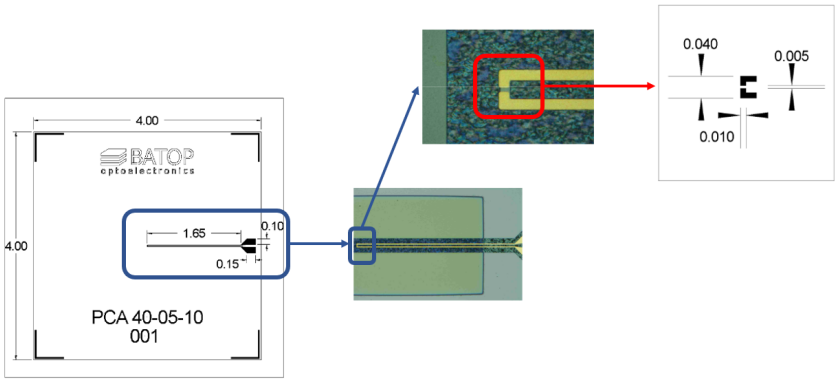

Figure 3.5: The Structure of PCA-40-05-10-1550-h antenna (dimensions are in mm)[3].

It can be seen that the it is a parallel line antenna with LT-InGaAs semiconductor material. Required optical excitation wavelength is $\sim$ 1550 nm. The size of the antenna chip is 4 mm x 4 mm, the antenna length is 0.040 mm, its width 0.01 mm and the antenna gap is is 0.005 mm.

On one side of the PCA chip, there is an aspheric lens in order to focus the excitation beam onto the antenna gap. On the other side at which the THz beam is emitted,

a hyperhemispherical undoped high resistivity float zone silicon (HRFZ-Si) lens is placed for THz beam guiding during emission. The whole structure is placed inside an aluminium case which acts as a heat sink. In addition, the PCA is also fixed inside a rotation mount in order to achieve a $360°$ of freedom to obtain a better focus and the desired polarization states. Figure above shows the lenses on the PCA and rotation mount.

(a) Aspheric lens. (b) Hyperhemispherical HRFZ-Si lens.

Figure 3.6: PCA with lenses and rotation mount.

In photoconductive antennas, providing a well focused laser beam incident on the antenna chip is important. In order to achieve this, the rotation mount of the PCA is attached to a mirror mount which provides tilts in three different axes. Finally, the piece which consists of PCA rotation mount and the mirror mount is fixed to an XYZ stage to allow movements in X,Y and Z axes. With all these degrees of freedom, the antenna is positioned so that its resistance value which is simultaneously measured using a multimeter by connecting the BNC cable of the antenna to it, is at a minimum. Acquiring the smallest possible resistance indicates the maximum illumination at the antenna gap which in turn implies the start of THz emission. As the last step, in order to achieve P polarized emission, PCA is rotated so that the the electrodes are aligned in the same direction as the laser source polarization as shown in Figure 3.7.

After the aligning the antenna for the lowest resistance, the PCA-multimeter connection is removed and the BNC cable of the antenna is connected to RIGOL DG2041A function generator. A bias voltage of ± 5V in the form of a square wave with a 1 kHz

frequency is supplied by the function generator to the antenna for the generation of carriers. The function generator is also connected to SR850 DSP lock-in amplifier so that the bias function is also used as a reference signal.

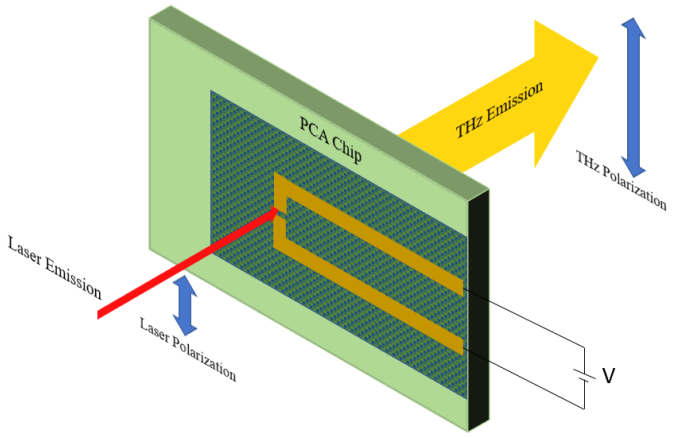

Figure 3.7: Illustration of THz emission polarization and electrode positions of PCA-40-05-10-1550-h.

On the detection side of the system, a BATOP PCA-100-05-10-1550-h is used. It is a bow-tie antenna which uses LT-InGaAs absorber to detect incoming THz signals. Its structure is shown in Figure 3.8. The chip size is 4 mm x 4 mm, the antenna length is 0.1 mm, its width is 10 μm and the antenna gap distance is 5 μm. The structural properties of the emitter and the receiver antennas are the same. The antenna chip is placed inside an aluminium case which works as a heat sink. The aspheric and hyperhemispherical HRFZ-Si lenses are placed on both sides. The holder used for alignment purposes is exactly the same. The same number of degrees of freedom is provided for the detector antenna. The resistance value which is measured using a multimeter is also reduced to be a minimum by focusing the laser beam onto the PCA gap through optical alignment. In order to measure the signal output which is an alternating current, the SR850 DSP lock-in amplifier is connected to the detector using a BNC cable.

The next step after setting up the antennas is to put off-axis parabolic mirrors (PM1-PM4) which are used to guide the THz beam from the emitter to the detector in the system. However, placement of the mirrors is heavily dependent on the properties and the position of the Si prism used in the system.

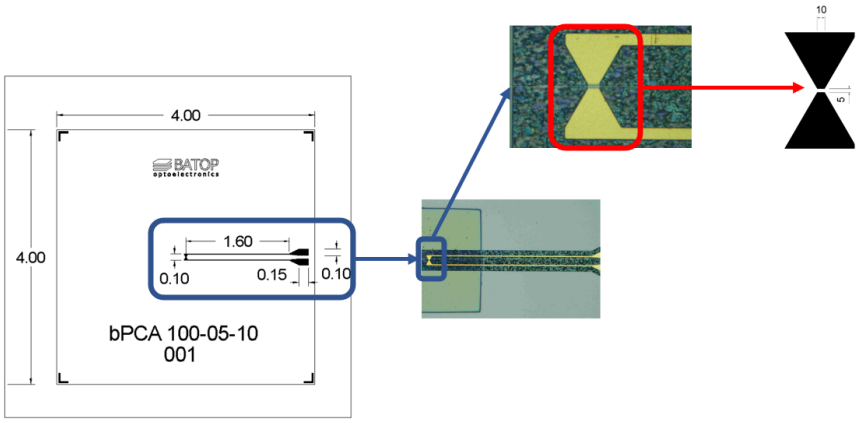

Figure 3.8: The Structure of PCA-100-05-10-1550-h antenna (dimensions are in mm and μm)[4].

Similar to the antennas, all four parabolic mirrors are attached to mirror mounts and also fixed to XYZ stages as shown in Figure 3.3. The position of PM1 is set to have the PCA chip at its focal point so that the incident THz beam which propagates by spreading out is thought to be emitted from the mirror focus. Therefore, the THz beam is perfectly collimated and folded by $90°$. PM2, on the other hand, accepts the collimated light and focuses it while again folding the beam by $90°$ at the same time. PM3 and PM4 act similarly, the light focused by PM2 is collimated by PM3 and sent to PM4. Then it is focused on last time by PM4 onto the PCA chip which again is set to be at mirror focal point. PM1 and PM4 mirrors have a focal length of 50.8 mm and a diameter of 50.8 mm. PM2 and PM3 mirrors have a focal length of 119.4 mm and a diameter of 63.5 mm.

3.3 GUIDING THZ BEAM AND OPTICAL PATH ANALYSIS

After passing through a focusing lens or reflecting from an off-axis parabolic mirror, the incident THz beam will propagate towards the ATR prism while getting converged on the focal point of the focusing optical element. In an ideal case, the THz beam will be refracted as it moves into the prism and a focused beam spot will appear at the center of the base of the Si prism. Then it will be reflected due to TIR and leave the prism.

It is very important to precisely guide the incident THz beam into the Si prism. Even a small mistake or a miscalculation causes serious errors in measurements and therefore in optical characterizations of materials. In addition, the configuration used to guide the THz pulse through the Si prism to achieve TIR is also an important factor for sample measurements and sample preparation as it directly affects the measurable minimum and maximum refractive indices and in turn, the penetration depth of the evanescent wave at the prism-sample interface.

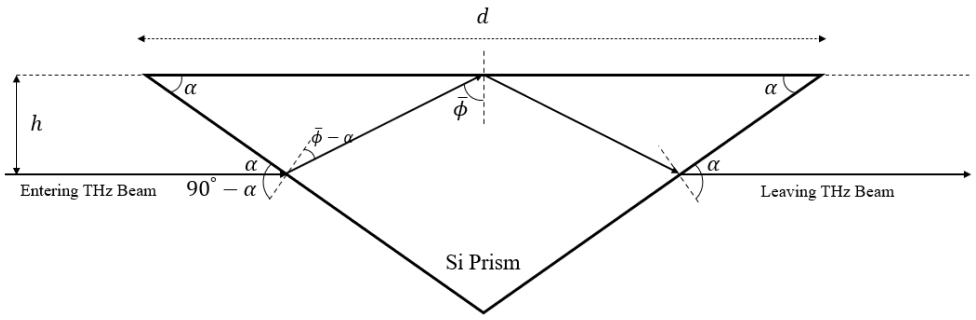

Figure 3.9: Cross Section of the ATR prism where $\alpha = 38.4°$.

Figure 3.9 above is a simple illustration of the path THz beam takes outside and inside of the Si prism in the experimental setup. It can be seen that the entering and leaving THz beams are parallel to the base of the prism. This configuration is decided after calculating the measurable refractive index range for many different incidence angles and parallel incidence provides the widest range. Parallelism of THz beams is achieved as a result of precise placement of PM2 and PM3 mirrors. Calculation steps of the measurable refractive index range for parallel incidence is as follows.

As stated above, the entire system is critically dependent on the incidence angle α. Any change in this angle affects the angle of incidence $\overline{\phi}$ at the base and changes the types of samples which can be measured with this system. Therefore, a very careful approach is required. In order to calculate the angle $\overline{\phi}$, the first step should be to find the angle $90° - \alpha$ which will be called β for convenience. Since the system is designed to send incident THz beam parallel to the base and the angle α known as it is determined by the design of the prism, by using the fundamental geometrical properties β angle is easily calculated.

$$\beta = 90° - 38.4° = 51.6° \tag{3.1}$$

Using β and Snell's Law, the angle labelled as $\overline{\phi} - \alpha$ is found. Again for convenience, this angle will be labelled as ω.

$$n_{air} \sin\theta = n_{prism} \sin\omega \tag{3.2}$$

$$\sin 51.6 = 3.42 \sin\omega \tag{3.3}$$

$$\omega = sin^{-1}\left(\frac{\sin\ 51.6}{3.42}\right) \tag{3.4}$$

$$\omega = 13.2° \tag{3.5}$$

Where n_{air} and n_p are the refractive indices of air and the prism and their values are 1 and 3.42 respectively. Then by applying the fundamental geometrical rules, the value of $\overline{\phi}$ is simply found as

$$\overline{\phi} = \omega + \alpha. \tag{3.6}$$

$$\overline{\phi} = 13.2 + 38.4 = 51.6° \tag{3.7}$$

In Chapter 2, the condition to achieve TIR is defined and introduced as follows.

$$\overline{\phi} > \overline{\phi}_C \tag{3.8}$$

Applying the formula given in Eq. 2.35 to calculate $\overline{\phi}_C$ gives

$$\overline{\phi}_C = sin^{-1}\left(\frac{n_{sample}}{3.42}\right) \tag{3.9}$$

Where n_s is the refractive indices of samples to be measured. Combining Eqs. 3.8 and 3.9 results in

$$\overline{\phi} > \overline{\phi}_C = sin^{-1}\left(\frac{n_{sample}}{3.42}\right) \tag{3.10}$$

As explained previously, Eq. 3.10 indicates that there is an upper limit for refractive indices which can be measured by the THz ATR-TDS system. It is because after a certain n_s value, the condition given above fails and the incident THz beam propagates directly into the other side of the reflection interface resulting in no total internal reflection.

Calculated refractive index measurement limit is given below.

$$1 \leq n_{sample} \leq 2.68 \tag{3.11}$$

Any sample with refractive index inside this range will be successfully characterized and optical properties will be discovered with the constructed THz ATR-TDS system. Defining a measurement window makes it possible to calculate penetration depth of the evanescent wave for measurable refractive indices. Using Eq. 2.53, penetration depth values plotted as shown below.

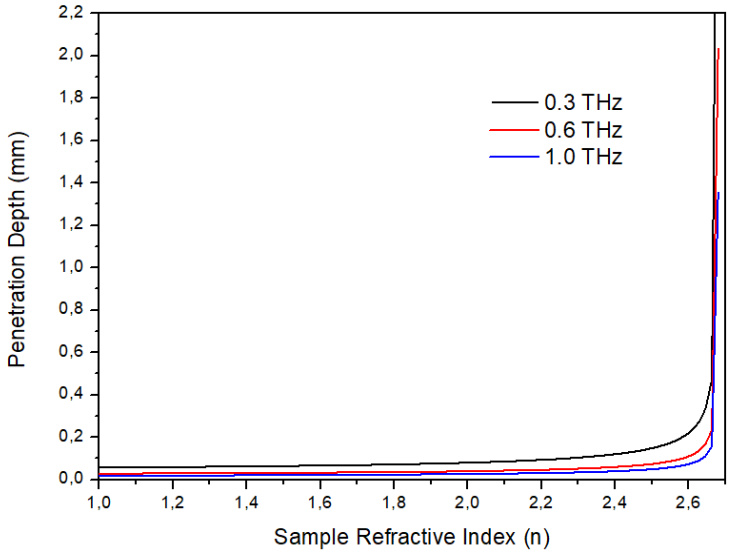

Figure 3.10: Penetration depth at 0.3, 0.6 and 1 THz in terms of measurable refractive indices of samples calculated using MATLAB.

There are two other important factors that limit the freedom of placing Si prism. One is the diameter of the beam before it enters the prism and the other is the distance it travels inside. The diameter of the incident THz beam should be small enough to allow the entire beam to pass into the prism without any losses due to being too large and forming a bigger spot than the lateral face of the prism it enters through. Therefore, the closest distance at which the prism can be placed with respect to the focusing optical element (PM2) must be the distance the THz beam forms a spot which is smaller than the lateral dimensions of the prism. In order to find this optimum distance, beam profile of the the THz emission after the antenna is investigated with the help of ZEMAX Optics Studio software. The optical structure of the emitter antenna, its emission profile and the beam spot properties at 50.8mm which is equal to the distance between the first parabolic mirror (PM1) and the antenna chip located behind the hyper-hemispherical lens is obtained as shown in Figure 3.11.

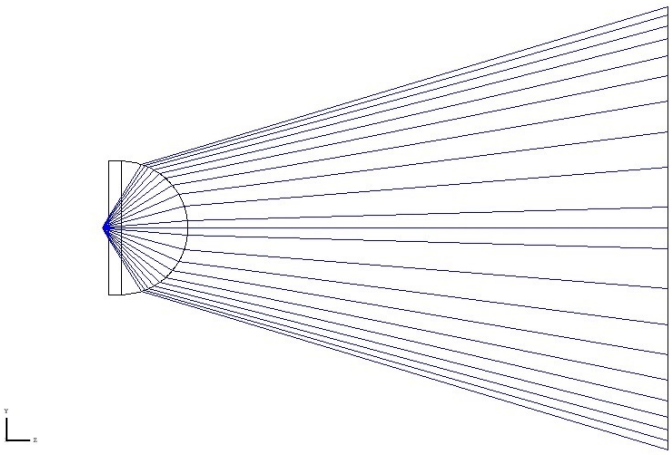

Surf:Type		Radius	Thickness	Glass	Semi-Diameter	
OBJ	Standard	Infinity	0.600	3.38,0.0	0.000	
*	Standard	Infinity	7.100	3.40,0.0	1.000	U
2*	Standard	-6.000	43.100		6.000	U
IMA	Standard	Infinity	-		19.927	

Figure 3.11: Emission profile and the spot size of the THz beam

The results show that the spot radius at the aforementioned distance is 19.93 mm. Using this information, optimum position for the Si prism can be determined.

In order to place the Si prism into the system, between the focusing parabolic mirors, a prism holder which is fixed on an XYZ stage is designed and 3D printed. Figure 3.12 shows the designed prism holder.

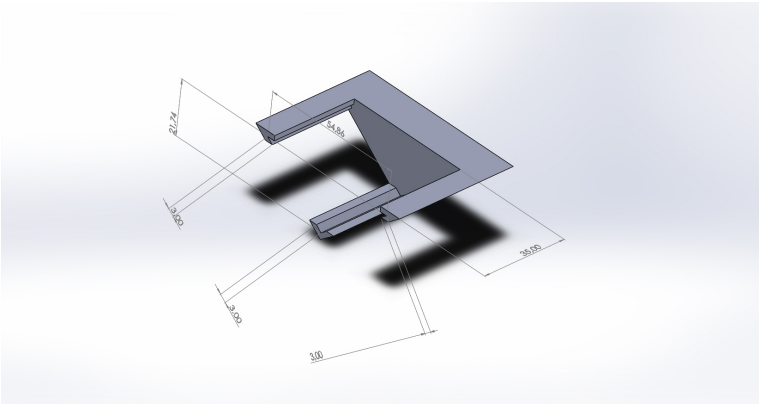

Figure 3.12: Prism holder structure designed by using SolidWorks software.

The lateral faces of the Si prism used in the system are squares with a side length of 35 mm as given previously. When put inside the holder, 3 mm of the lateral surfaces

from the top and the bottom are covered by the structure. As a result, the dimensions become 29x35 mm and the widest beam spot radius allowed to propagate inside the prism reduces to 14.5 mm. In order to prevent any possible errors, the spot radius is set to be 14 mm.

A sketch of the two off axis parabolic mirrors (PM1 and PM2) and the emitter antenna used in the system is given in Figure 3.13. The first step is to calculate the angle of convergence of PM2 which has a focal length of 119.4 mm. Convergence angle makes it possible to find the focused spot size at different positions with respect to the mirror.

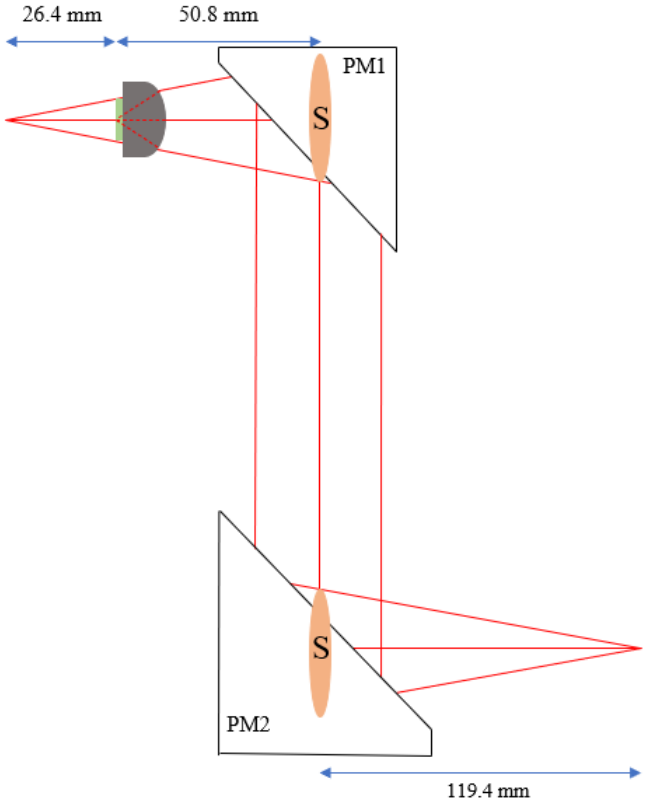

Figure 3.13: Behaviour of the emitted THz beam collimated and focused by parabolic mirrors PM1 and PM2.

Spot radius at PM1 is given above and therefore the spot radius of the incident THz beam at PM2 is known since the two are the same.With a known focal length and a spot radius, the calculation of the convergence angle of PM2 becomes quite straightforward.

$$\theta_{conv} = arctan\left(\frac{19.93mm}{119.4mm}\right) = 9.47° \tag{3.12}$$

$$d = \frac{14mm}{tan(9.47)} = 83.93mm \tag{3.13}$$

$$D = (f - d) = (119.4 - 83.93)mm \tag{3.14}$$

$$D = 35.47mm \tag{3.15}$$

Where f is the focal length of the PM2 and D is the distance from the mirror. The result shows that after approximately 3.5 cm away from the PM2, the spot radius of the focused THz beam becomes small enough to completely propagate inside the Si prism. As expected, the distance to PM3 at the other side is also set to be the same as the distance to PM2.

Finally, after obtaining a safe distance which allows THz beam to completely go inside the prism without any losses caused by spot size, one last factor remains to finalize the placement process. It is the optical path length (OPL) of the light inside a medium. A beam of light, travelling a certain distance inside a medium takes an optical path usually longer than it is estimated in air. The length of the path light takes inside a medium which is the Si prism in this case is given as

$$S = n_{prism}.s \tag{3.16}$$

Where s is optical path of the light in air, S is geometrical distance the light travels inside the medium and n_{prism} is the refractive index of the Si prism. Figure 3.14 is a representation of the Si prism and its geometrical properties.

The first thing needed to calculate is the distance S. Calculation is purely based on geometrical principles, therefore it is skipped. Following Eq. 3.16 gives

$$S = 17.498mm \tag{3.17}$$

$$17.498 = 3.42.s \tag{3.18}$$

$$s = 5.116mm \tag{3.19}$$

Results above show that the incident THz beam will have to travel $17.498mm$ geometrically inside the prism so that the focal point is located exactly at the base where, as mentioned previously, the samples are placed.

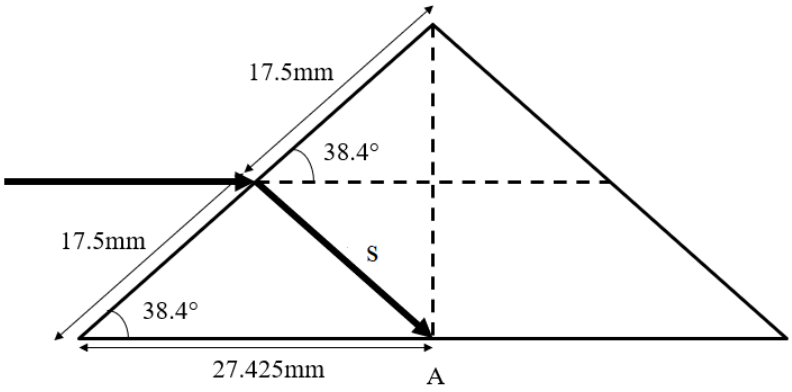

Figure 3.14: Geometrical representation of the Si Prism.

In order to achieve this length optically, only $5.116mm$ of the focused incident THz beam must go inside. Focusing mirrors used in the system have a focal length of $119.4mm$. Using this information, the distance between the point on the prism where the incident THz signal enters and the focusing parabolic mirror is calculated as

$$s = 5.116mm \tag{3.20}$$

$$f = 119.4mm \tag{3.21}$$

$$l = 119.4 - 5.116 = 114.284mm \tag{3.22}$$

Comparing this result with the value given in Eq. 3.15 shows a great safety for placing the Si prism at this calculated point since the spot size of the focused incident THz beam will already be small enough to propagate inside the Si prism without any losses. Although everything seems perfect in theory, putting the prism in its correct position is a challenging task since measuring the aforementioned distance is quite difficult as this calculated distance corresponds to the space between the center of the mirror and the middle point of the prism's lateral face. In order to overcome this difficulty, the distance from the center indicator (sticky tape) of the focusing mirror (PM2) to the edge of the prism holder is set to $94.83mm$ as explained in Figure 3.15. The necessary calculations are basic geometry, therefore omitted.

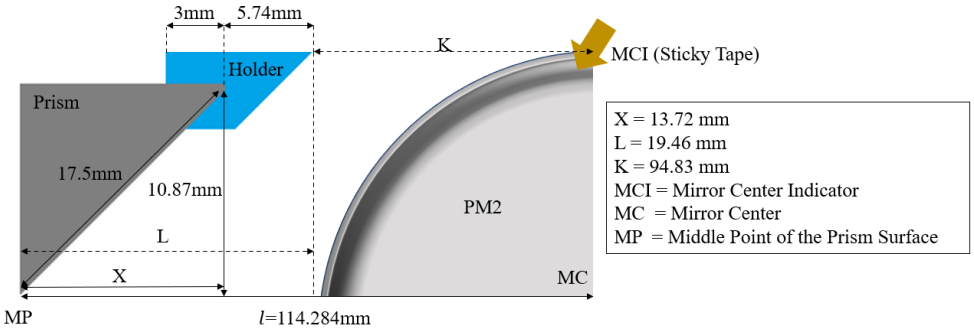

Figure 3.15: Holder to mirror center indicator distance.

After setting up the entire system, THz beam is focused on the base of the prism with an incidence angle $51.6°$ and a focal spot size of 4 mm. The location of the focal point is marked by a pointer laser on the outside to help with sample placement during measurements. It is critically important to have a spot size as small as possible because the spot size at the focus of the THz beam determines spatial resolution of the system. THz pulse and the power spectrum measured after being reflected from the prism are shown in Figure 3.16 and Figure 3.17, respectively. This THz pulse has a bandwidth up to 1 THz with a SNR of $1000:1$.

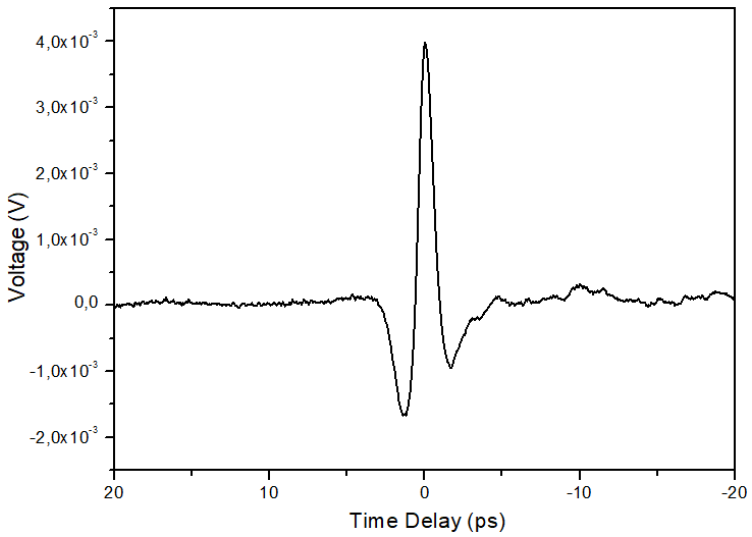

Figure 3.16: Waveform of the first THz signal obtained from the system in time domain.

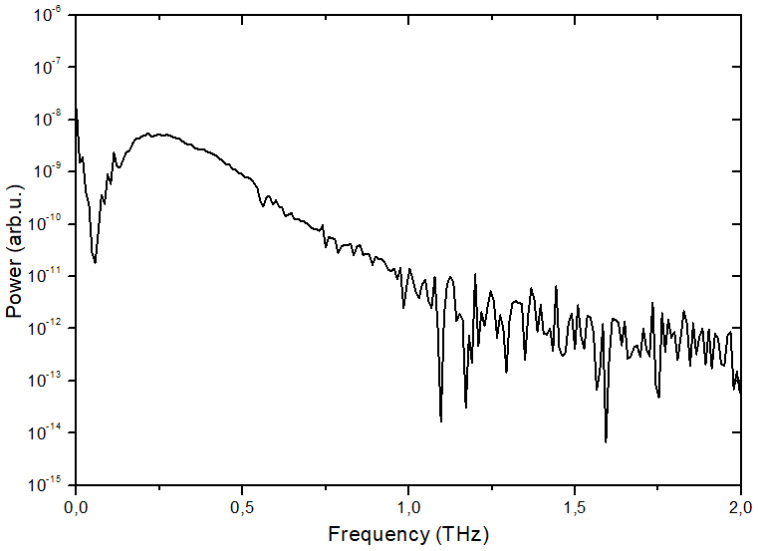

Figure 3.17: Power spectrum of the first THz signal.

3.4 DATA ACQUISITION AND ANALYSIS

Data acquisition in the system is executed by a software previously coded in Labview. The software establishes a communication between the translational stage controller and the lock-in amplifier so that during measurement, the software records the value of the THz signal taken from the lock-in amplifier output at each translational stage step which corresponds to a predefined time interval and constructs the entire waveform in time domain.

The results are immediately shown on the screen without needing any additional steps. Therefore, the user can easily evaluate the measurement quality and repeat the measurement if necessary without losing time. The software also lets the user to set the scan distance, step size and the time interval between steps of the translational stage to desired values for more detailed, longer and slower measurements or vice versa. Measurements in this thesis were generally set to 10 μm step size and 300 ms wait time between each steps and . That is, the translational stage moves 10 μm and waits at that step for 300 ms while recording THz signal amplitude. Then it moves to the next step and repeats the same procedure until the preset scan distance is reached.

The analysis of the recorded THz data is done by using both Origin Pro. 8 and MATLAB software. First, excess data deleting and zero-padding process is applied to time domain signal in order to obtain better and accurate results. Then this processed data is used in FFT calculations done by using either Origin Pro 8 or MATLAB. After obtaining FFT results, the measured signal (both reference and sample) goes through the mathematical process explained in Section 2.2.3 and plotted to reveal optical characteristics of the measured sample.

CHAPTER 4

MEASUREMENTS WITH THE THZ ATR-TDS SYSTEM

In this thesis, a time domain spectroscopy system based on total internal reflection principle was developed for optical characterization of highly absorptive samples. In this chapter, the first part explains properties of samples investigated for this research. Then in the second part, ATR spectroscopy results of the samples are given in order to determine the efficiency of the system and the technique proposed in this thesis. Finally, the chapter ends with a discussion about the obtained outcome and the eligibility of the THz ATR-TDS system.

4.1 SAMPLES

In this study, two different, but still related, types of samples were measured and the results are presented in this thesis. The first sample is distilled water taken from a container kept in the Terahertz Research Laboratory at METU. A drop of distilled water which was spread out to have approximately 5 mm width was carefully placed directly on top of the ATR prism using a stactometer and with the help of a marker laser.

The second sample type is biological tissue samples which are 5 mouth tissue slices containing different types and amounts of lesions taken from patients with their consent and ethical approval from the Faculty of Dentistry of Ankara University. Similarly, tissue samples were placed directly on top of the Si prism during measurements. In order to make sure that the samples were fully in contact with the prism surface, each sample were flattened as possible while avoiding damaging the tissue. Figure 4.1 and 4.2 show the measured water and tissue samples respectively.

Figure 4.1: Water sample on the Si ATR prism surface. The bright red light is the marker laser spot.

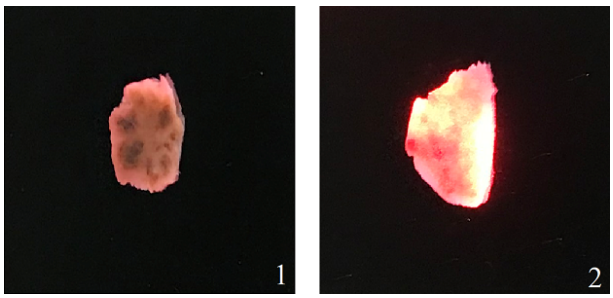

(a) Tissue samples 1-2.

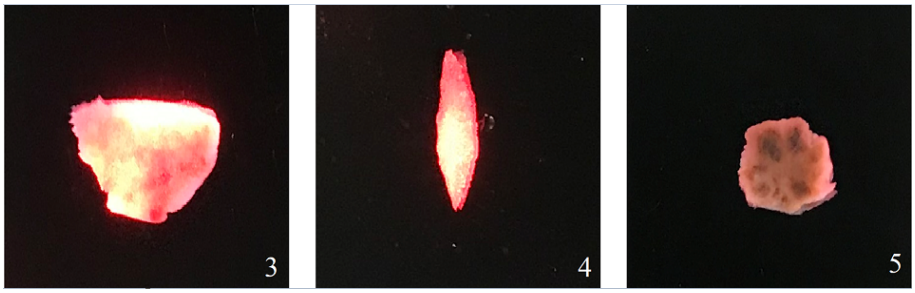

(b) Tissue samples 3-5.

Figure 4.2: Mouth tissue samples on the Si ATR prism surface. The bright red glowing is due to the marker laser spot.

4.2 TERAHERTZ ATR SPECTROSCOPY RESULTS

4.2.1 TERAHERTZ ATR SPECTROSCOPY RESULTS OF WATER SAMPLE

Absorptive characteristics of samples due to the imaginary parts of their refractive indices result in attenuation in the signal amplitude with respect to reference measurements in time domain. The decrease in the signal becomes more obvious with water since it has a very high absorption. Analysis of this amplitude difference reveals optical properties of water in terahertz region.

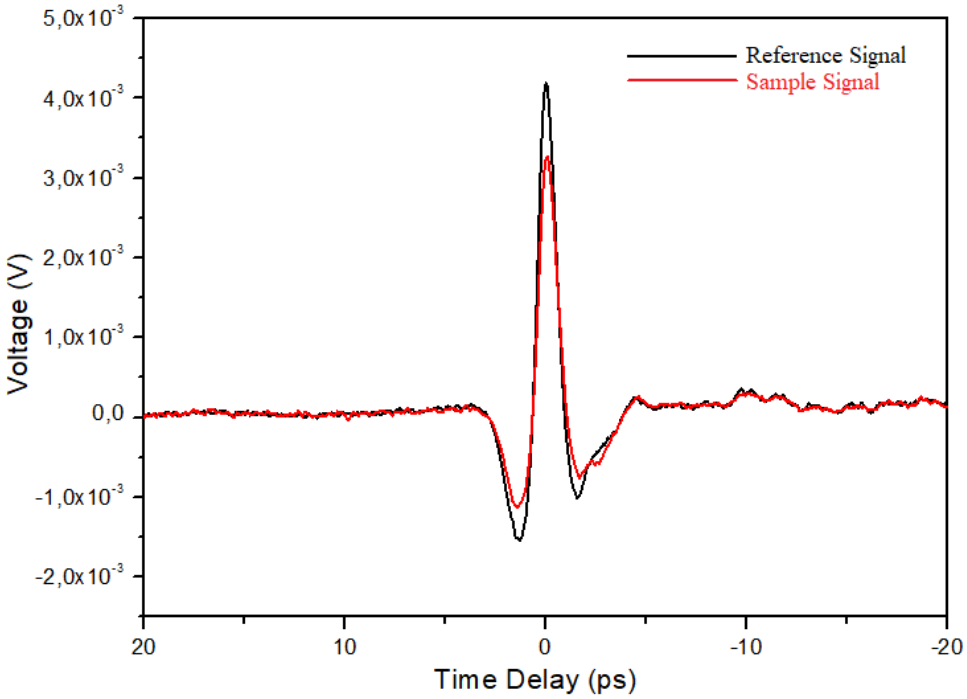

Figure 4.3: Reference and sample signal measured using the constructed THz ATR-TDS system.

Figure 4.3 shows the time domain measurement results of water sample. Reference THz signal, shown as a black line, obtained with nothing on top of the ATR prism and it has a peak at 4.19 mV. Sample signal, the red line, is obtained with water placed at the prism surface as shown previously in Figure 4.1. Its peak is at 3.25 mV. Each measurement took approximately 8 minutes. Even before going through the analysis

process, the biggest advantage of the ATR-TDS method which was emphasized repeatedly throughout this thesis can be understood from the time domain results alone. Instead of losing it nearly completely to water absorption, the THz ATR-TDS system was able to record a high percentage of the THz signal with a reasonable attenuation of 94mV as expected.

Analysing time domain results by following the steps explained in section 2.2.3 and using Eqs. 2.57-2.67 gives two important results used in optical characterization of materials. One is the refractive index of the sample in THz region.

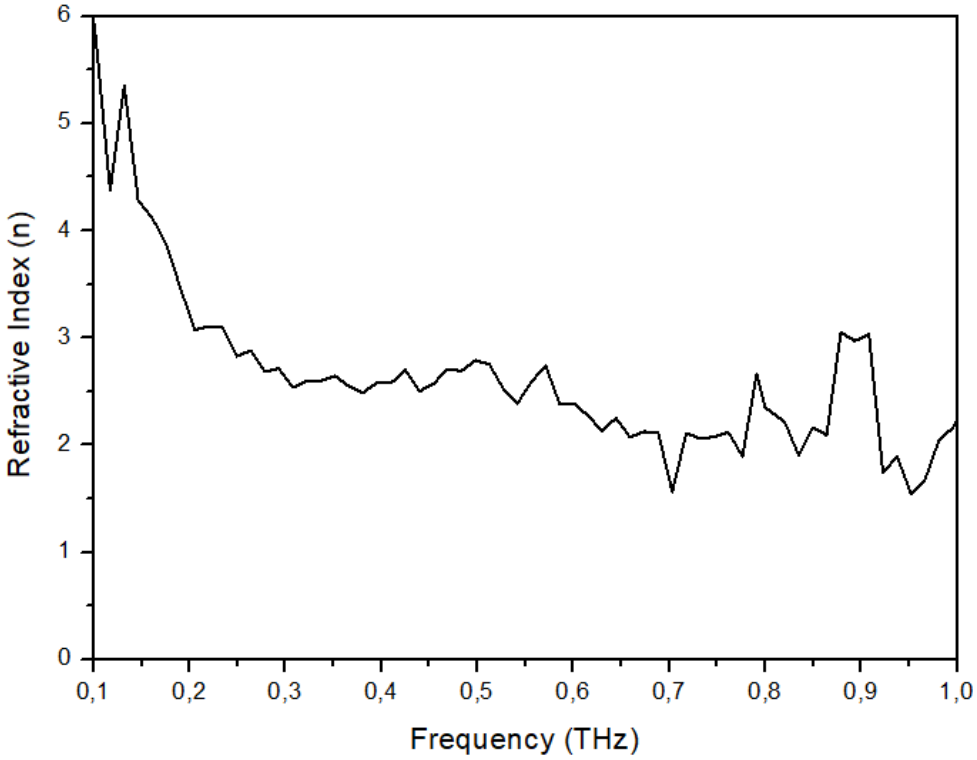

Figure 4.4: Refractive index of water up to 1 THz.

Figure 4.4 shows refractive index analysis results of water. In full bandwidth range of the system, it is seen that the refractive index curve reaches approximately to 2.16 at 1 THz. In general, results look consistent except points between 0.65 and 0.95 THz.

The other outcome obtained after applying the procedure given previously to time domain results is the absorption coefficient of samples. Figure 4.5 below shows calculated absorption coefficient of water up to 1 THz.

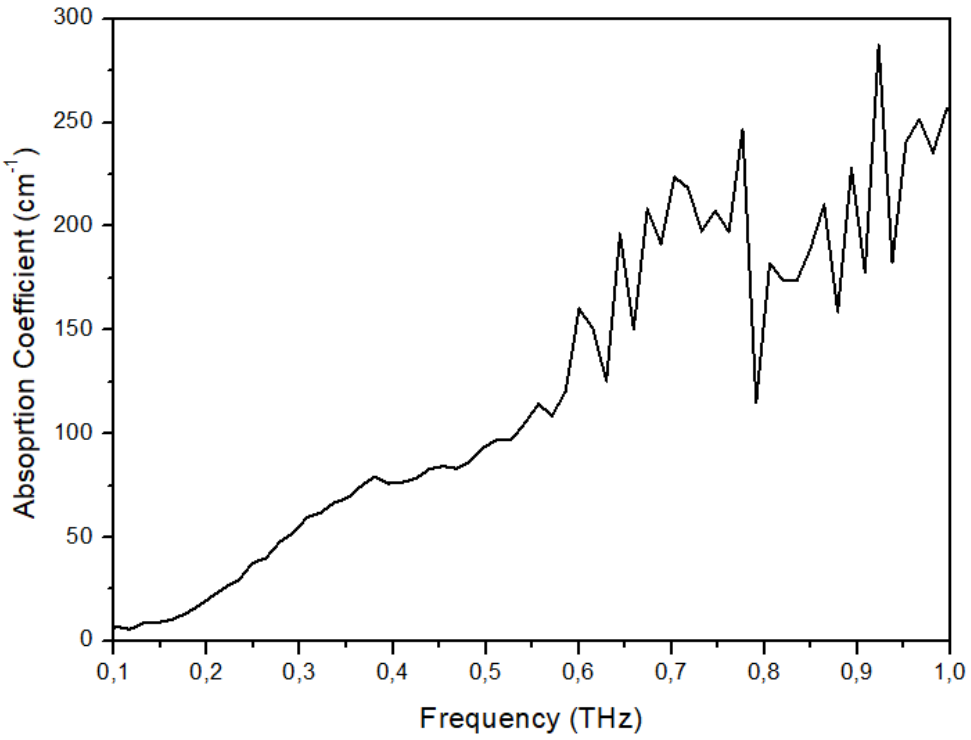

Figure 4.5: Absorption coefficient of water up to 1 THz.

Starting from 0.1 THz up to 1 THz absorption coefficient curve again looks consistent expect between 0.65 and 0.95. At 1 THz, the absorbtion coefficient is found to be approximately 250 cm^{-1} for water.

4.2.2 TERAHERTZ ATR SPECTROSCOPY RESULTS OF TISSUE SAMPLES

Shortly after completing water sample measurements, the constructed THz ATR-TDS system has developed a technical fault and stopped working. Diodes inside the ultrafast laser source had burned and due to being on a tight schedule, waiting for replacements was not an option. Therefore, an entirely new THz-ATR-TDS system was constructed with a new laser source for tissue sample measurements in a short time. As a result, in the beginning of this section, technical properties of the new system will be briefly explained in order to preserve the consistency in given information.

The second system is based on electro-optic sampling method for THz detection explained in Chapter 1. A Yb-doped ultrafast laser which operates at 1040 nm and has

a 250 fs pulse duration is used as the laser source. THz generation is provided by a GaBiAs based PCA. THz pulses guided through the prism with two teflon lenses with f-numbers 1.5. Focused THz beam at the prism base has a radius of 2.5 mm. The system configuration regarding the behaviour of THz pulses inside the Si prism is exactly the same as the first system. Therefore, mathematical background explained in Chapters 2 and 3 apply to the second system without any changes. Figure 4.6 shows the second THz ATR-TDS system. In Figure 4.7, the THz waveform generated by the system and its power spectrum is given.

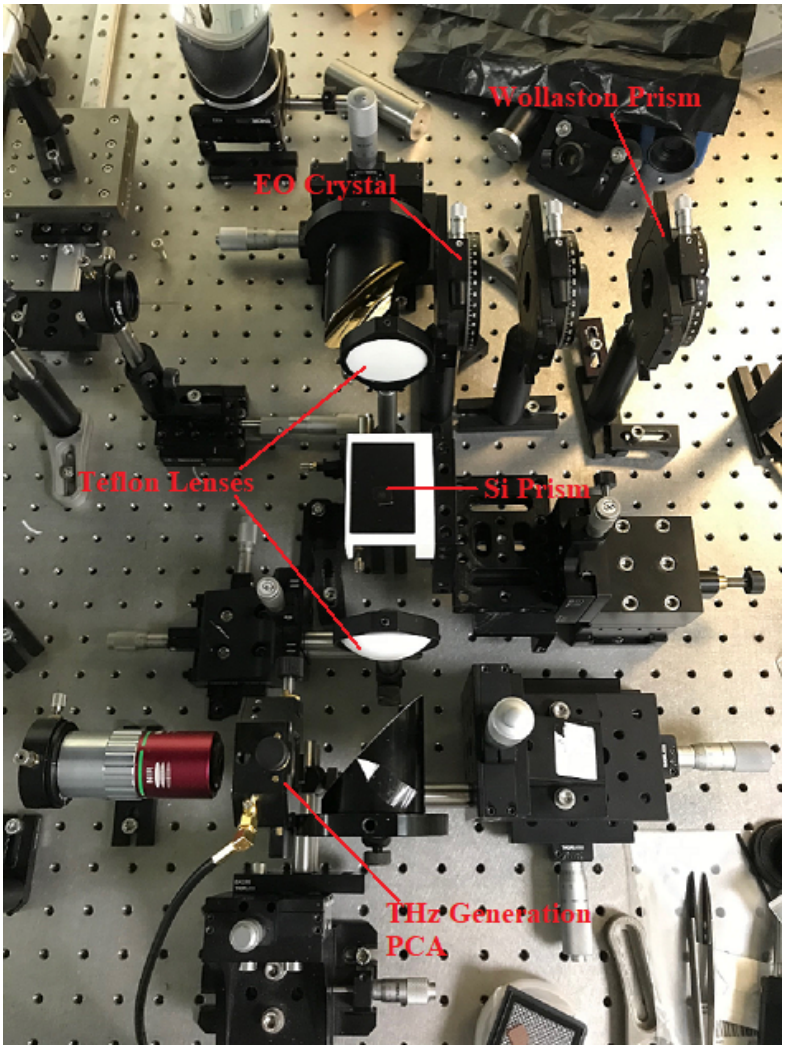

Figure 4.6: The second THz ATR-TDS system.

Power spectrum of the THz signal indicates that the bandwidth of the new system reaches up to 0.65 THz with SNR 1000:1. Although the signal to noise ratio is still good, compared to the first configuration, nearly half of the initial bandwidth is lost.

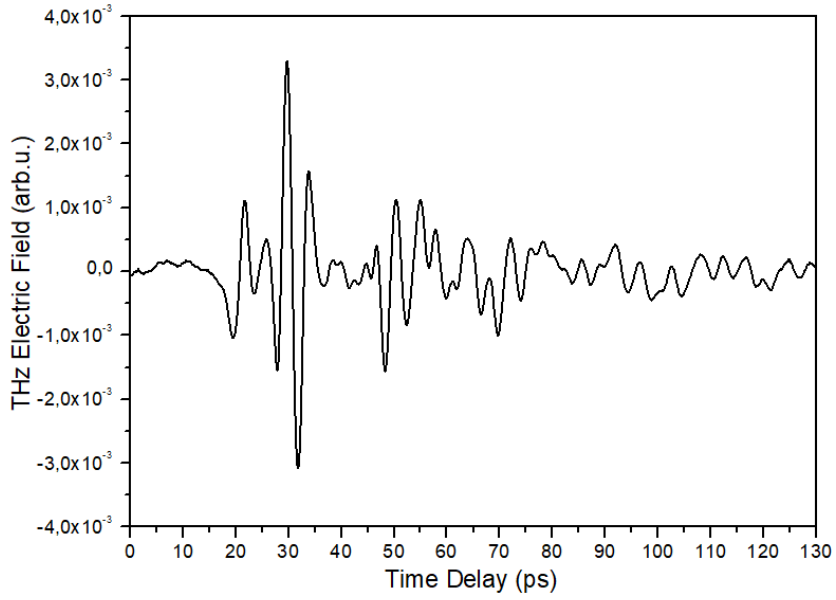

(a) THz waveform.

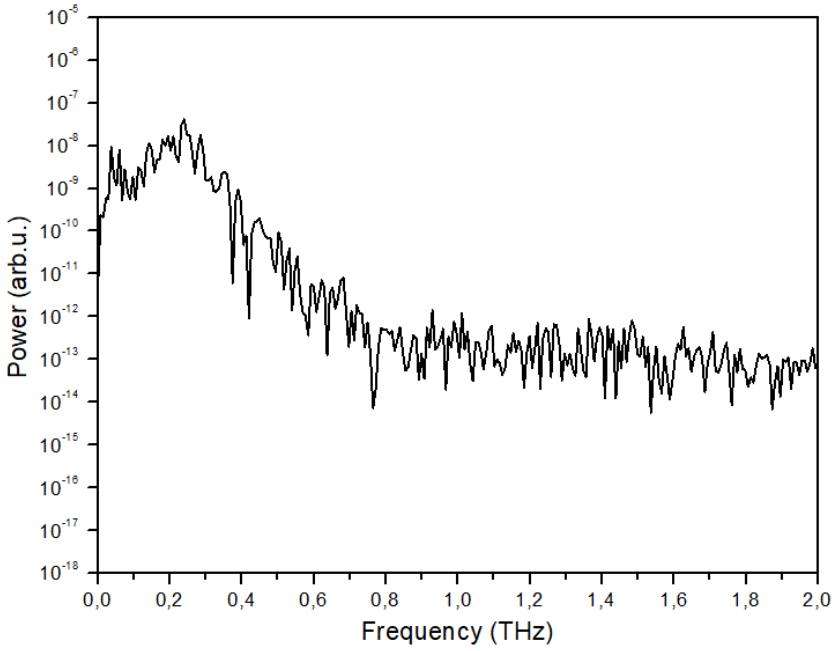

(b) Power spectrum.

Figure 4.7: THz waveform in time domain and its power spectrum recorded by the second THz ATR-TDS system.

Time domain measurements of 5 tissue samples with the new THz ATR-TDS system are given in Figures 4.8-4.12 on the next page.

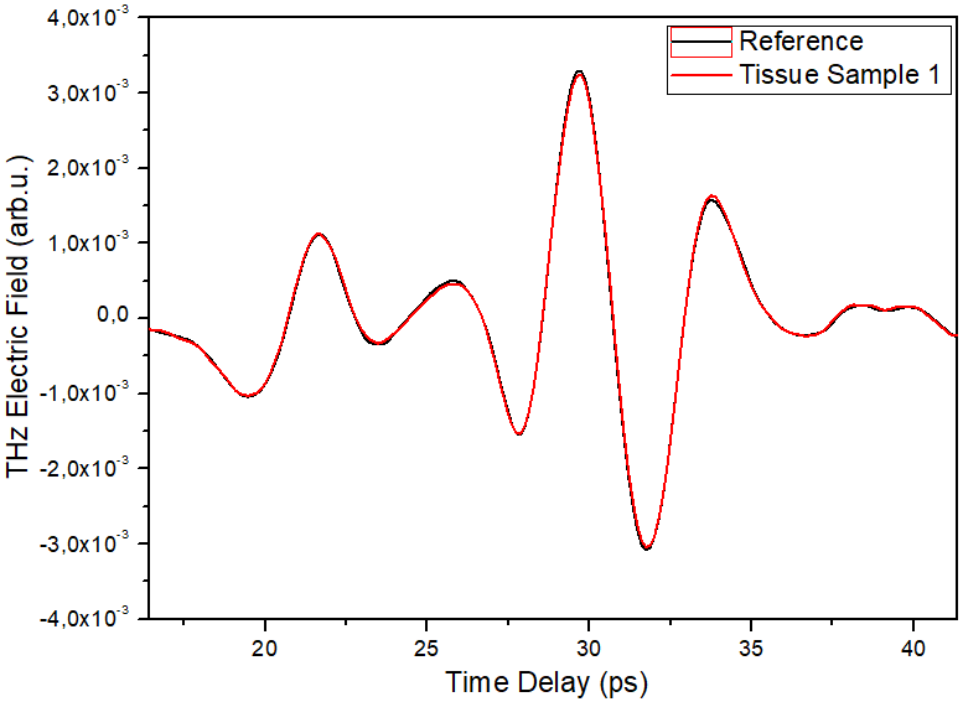

Figure 4.8: Tissue sample 1 time domain measurement. Peripheral giant cell granuloma.

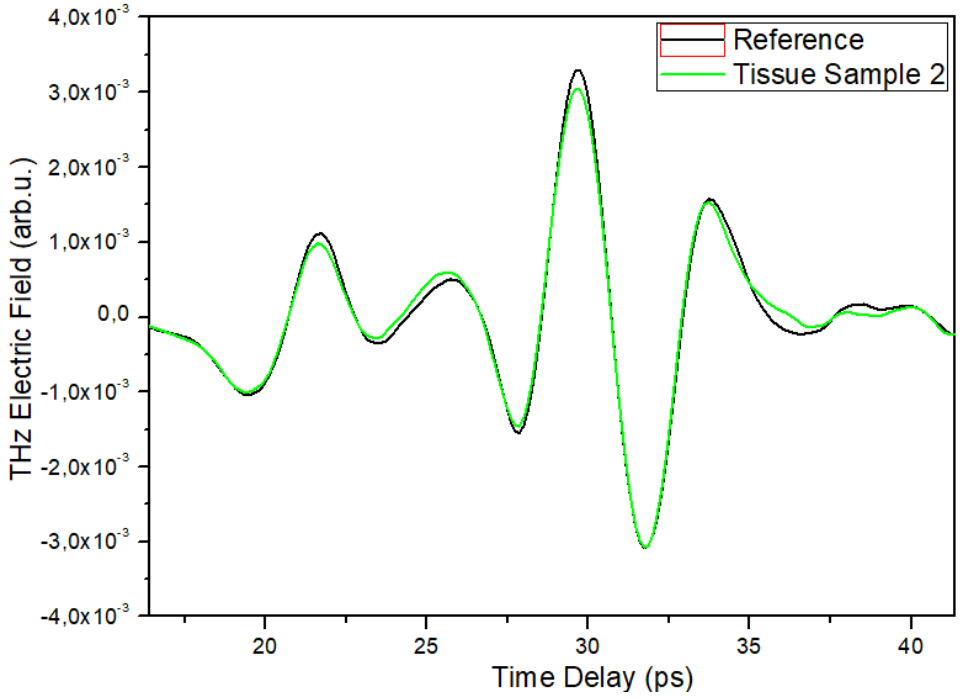

Figure 4.9: Tissue sample 2 time domain measurement. Peripheral giant cell granuloma.

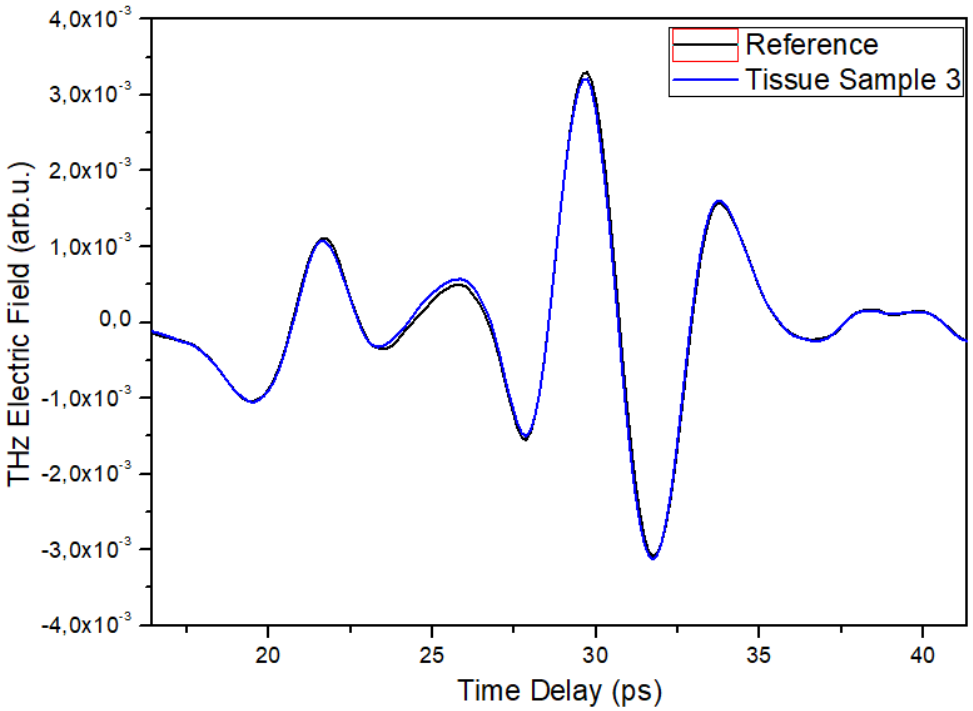

Figure 4.10: Tissue sample 3 time domain measurement. Pleomorphic adenoma.

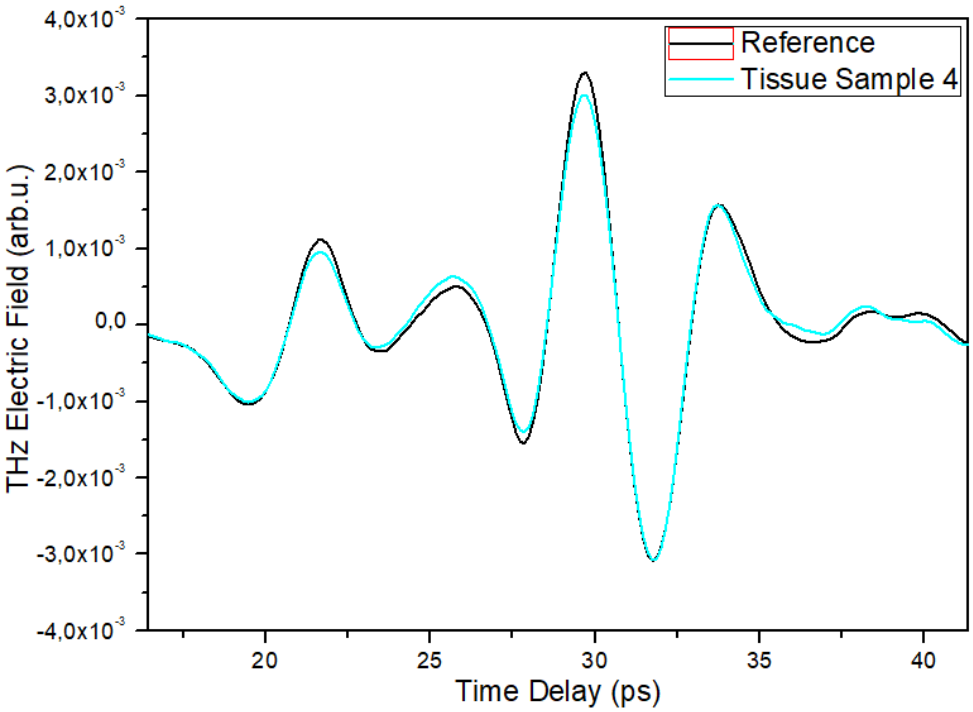

Figure 4.11: Tissue sample 4 time domain measurement. Fibrosis polyp.

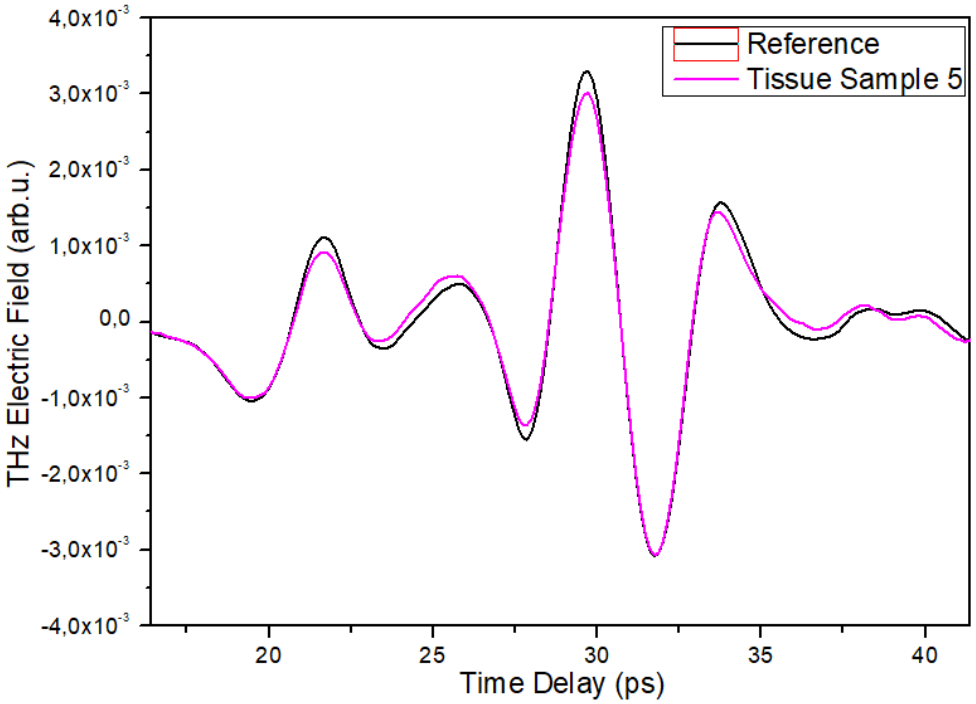

Figure 4.12: Tissue sample 5 time domain measurement. Fibrosis polyp.

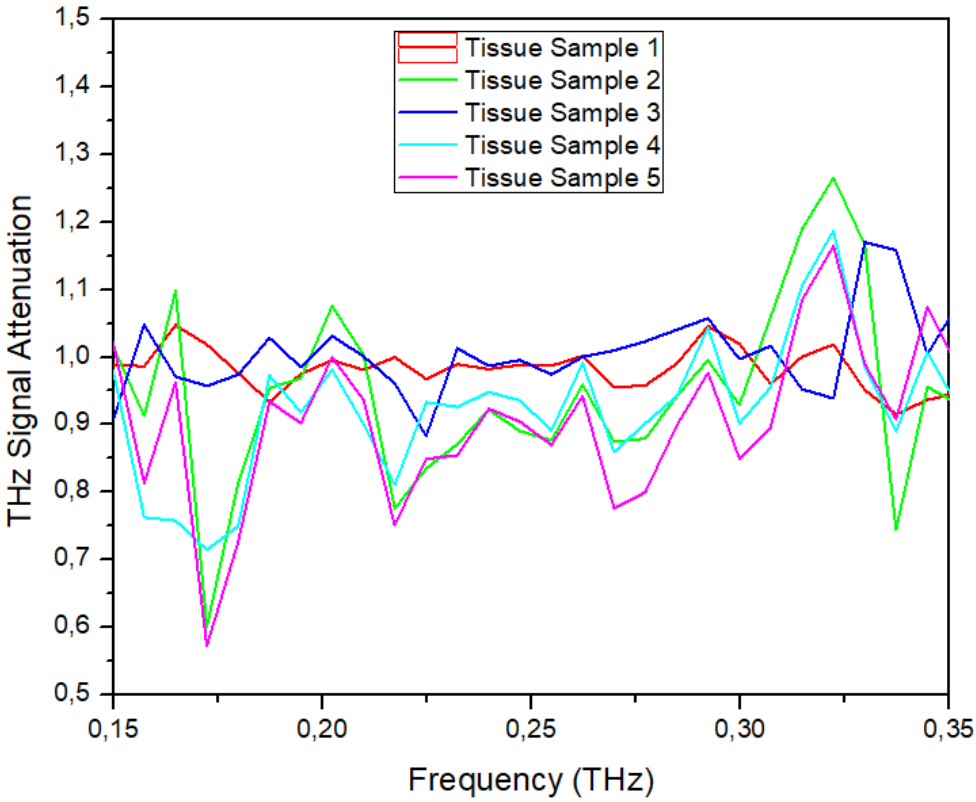

Figure 4.13: Signal attenuation analysis results.

Signal attenuation analysis of each measurement which is done by taking the power ratio of sample and reference signals obtained from the Fourier transformed data reveals the effective measurement window of the system in frequency domain. It corresponds to the frequency range in which the aforementioned ratio is less than 1. The results of this analysis is given in the Figure 4.13 and it is seen that the measurement window of the new system is between approximately 0.15-0.35 THz. The result of this very narrow measurement window makes it very difficult to go further in analysis. Attempts of extracting refractive index and absorption coefficient data does not give any meaningful results. In addition, lack of healthy tissue samples provided by the Faculty of Dentistry of Ankara University prevents comparing infected and healthy tissue measurements. However, even with the presented results, deductions can be made about the system performance and the efficiency of the THz ATR-TDS technique. Lastly, every tissue measurement result is given in a single plot in Figure 4.14 in order to show differences in amplitude and time scale between each measurement.

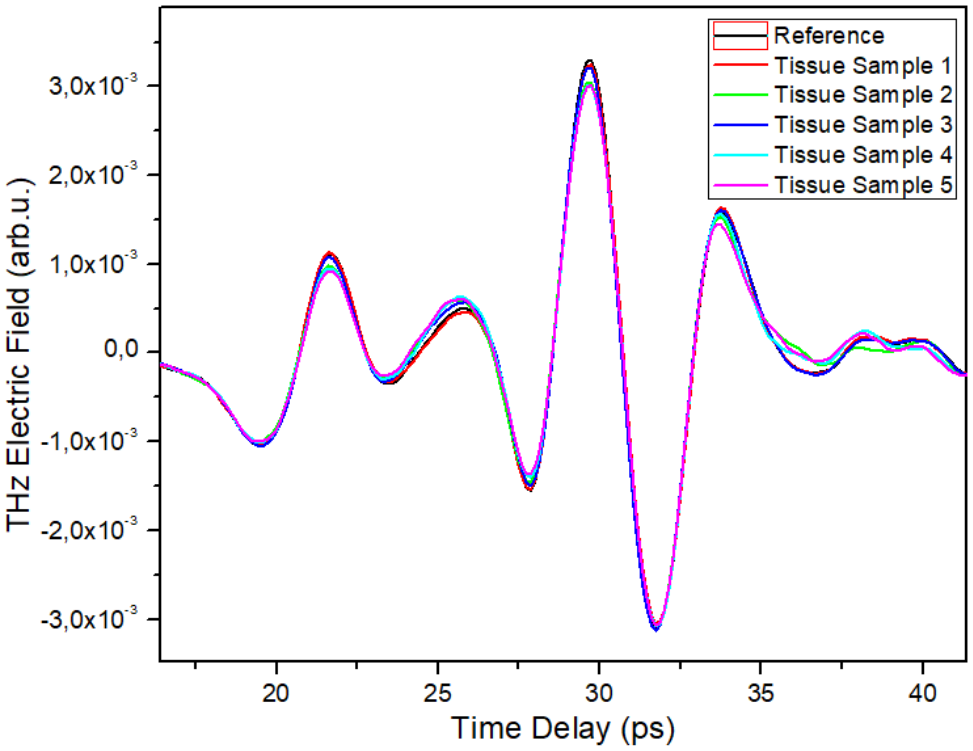

Figure 4.14: Every tissue measurement in a single plot.

4.3 DISCUSSION

4.3.1 WATER SAMPLE

The first sample investigated by the THz ATR-TDS system was distilled water sample. Measurements were done by the first experimental setup. In Figure 4.3 it is clear that the THz signal is not lost to water absorption. It is partially attenuated due to the imaginary part of the refractive index of the sample as expected. This is, as previously stated, the proof of success for THz ATR-TDS technique in absorptive sample analysis. Using this method, materials with high absorptive properties in THz region can be investigated while being minimally affected by the absorption.

The results of refractive index analysis given in Figure 4.4 for water seem to be generally in an agreement with literature values given in the works of Jepsen et al. [57], Nagai et al. [41], Soltani et al. [45] Moller et al. [38], Venables et al. [58], Naganishi et al. [44] and Hirori et al. [37]. In these studies, refractive index curves of water stabilizes around 2.1-2.4 and at 1 THz, they reach values between 2.3-2.1. Similarly, the refractive index curve for water given in this is thesis stabilizes around 2.3-2.1 and reaches 2.16 at 1 THz with some discrepancies between 0.65-0.95 THz.

Absorption coefficient analysis results of water shown in Figure 4.5 are in a general agreement with the given literature results too. Absorption coefficient curves given in reference studies mostly show a linear trend and reach around $250cm^{-1}$ at 1 THz. The absorption coefficient curve presented here behaves similarly and reaches approximately the same value at 1 THz with inconsistencies between the same frequency range as in refractive index curve.

A comparison between the literature and results of this study reveals that the constructed THz ATR-TDs system was successful in optical characterization of water and the theoretical method explained in previous chapters holds true. However, there are data points both in refractive index and absorption coefficient plots which does not agree with the references. The THz ATR-TDS system is highly susceptible to small deviations in guiding THz beams and other environmental factors. Especially the alignment of the Si ATR prism affects results greatly. Soltani et al. has shown

that a misalignment between $-0.05°$ and $0.05°$ changes refractive index results by ± 0.5 [45]. Therefore, the differences from literature results across the measurement frequency window can be explained by small misalignments in system. In addition, state of the THz focal point at the Si prism base is another critical point which affects measurement results. It is important to have the focus exactly at the prism surface. Focusing THz beams before or after the prism base does not cause any noticeable errors in signal levels or time domain results. However, when extracting optical properties, large errors usually indicate this problem and it could be given as another explanation for discrepancies in the results. In their study, Liu et al. explains that errors in sample placement, that is, missing the THz focal point so that a portion of the evanescent wave goes into air is one of the other reasons for errors in results [56]. In addition, samples should be completely in contact with the Si prism in order to prevent having air in between.

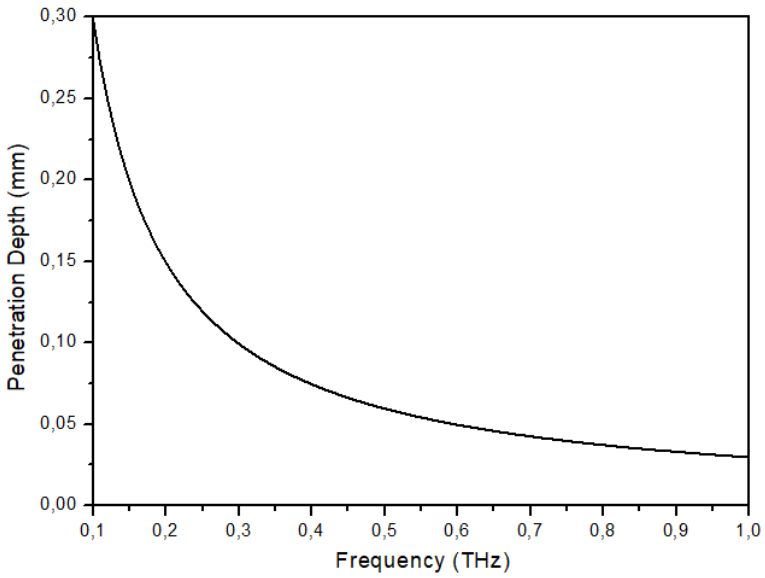

Figure 4.15: Penetration depth of THz evanescent wave for water from 0.1 THz to 1 THz. In this plot, water refreactive index is taken as 2.2.

When preparing samples, it is critically important to have sample thickness larger than the penetration depth of the evanescent wave inside the measurement window. For the water sample with thickness around 1 mm, penetration depth values are shown in Figure 4.15. It is clear that there were no errors caused by wrong sample thickness.

4.3.2 TISSUE SAMPLES

After proving that the THz ATR-TDS technique can successfully characterize high absorptive materials such as water. Samples containing water, especially biological samples could be optically characterized. However, due to the problem mentioned in previous section, in biological measurements new THz ATR-TDS was used. The new system has very narrow bandwidth and a narrower measurement window. Despite the disadvantages, given measurements in Figures 4.8-4.12 show that THz signal was not lost during measurements due to water absorption. This in turn reveals that under improved technical conditions, optical characterization of biological samples at THz frequencies, a measurement which required special sample preparation or took too much time and effort, can be done in a very short time without needing any specific sample preparation. It was stated before that each tissue sample contained different amounts and types of infected parts. The main purpose after showing that THz spectroscopy of biological tissues could be done successfully, was to be able to differentiate these infected tissues according to their optical properties. However, not receiving a healthy tissue and poor system performance prevented this analysis. Although the aforementioned analysis was not possible, when inspected together as shown in Figure 4.12, differences in signal level and time scale become visible. Signal level differences are thought to occur due to the imaginary parts of the refractive indices of samples. Time scale differences, on the other hand, could be linked to the real parts of refractive indices. These different refractive index values and therefore different time domain results of each sample could be caused by the contained infections. Different results between the same type of infections could be a result of different amount of infected parts. Specific response of each infection to THz radiation could be accounted for the differences in results between different types of infections. However, absence of healthy tissue samples weakens the strength of these arguments. Nonetheless, it could be deduced that the THz ATR-TDS method serves its purpose even under non-ideal conditions only by inspecting time domain measurement results as similarly shown in the studies which belong to Cherkasova et al. and Newnham et al. [59][60].

CHAPTER 5

CONCLUSION

In this thesis, a study of a new THz spectroscopy method called time domain terahertz attenuated total internal reflection spectroscopy or in short THz ATR-TDS is presented. The main purpose of the method is to be able to optically characterize highly absorptive materials such as water, aqueous solutions, other liquids and biological samples which contain high amount of water with large thickness in THz region of electromagnetic spectrum without losing the signal to absorption which is usually the case in transmission spectroscopy. First, theoretical background is given and then mathematical instruments which are required to explain the physics behind the process are provided in detail. A comprehensive explanation for the theory of light-matter interactions, behaviour of light and spectroscopy takes more than twice the size of this thesis. Therefore, only the essential points to help with understanding the experimental process are given in the following chapters.

Water and five biological samples which are mouth tissue samples containing different kinds and amounts of infected parts are investigated by using the constructed THz ATR-TDS systems. Water measurement is done by the fist experimental setup. The first system used an Er-doped ultrafast fiber laser alongside with InGaAs based emitter and detector PCAs provided by BATOP GmbH, Germany. Emitted THz radiation is first collimated and then focused inside a Si ATR prism by two off-axis parabolic mirrors placed on emission side and totally reflected at the prism base. After reflection, reflected THz beam is guided by the same off-axis parabolic antenna configuration on the detection side to be collected by the detector. Size of the focal point at reflection interface is measured to be approximately 4 mm. Bandwidth of the recorded THz waveform reaches up to 1 THz with a SNR of 1000:1.

Another advantage of THz ATR-TDS method is that it does not require a special sample preparation process. Water is measured by putting a drop of water on top of the Si ATR prism. Here, only factor which requires attention is correct sample placement and having thick and wide enough samples so that evanescent THz wave interacts with samples properly. When the presented measurement results are compared to literature results, it can be concluded that the constructed THz ATR-TDS system serves its purpose. A high percentage of THz signal is still preserved while being attenuated as expected. The differences between the reference and sample measurements in signal amplitudes and time scale are used to extract optical properties of water at THz frequencies. There are of course errors in results to some degree but they can be reduced by optimizing the system and improving measurement conditions.

Tissue sample measurements were done using another THz ATR-TDS system constructed due to technical problems with the first one. The seconds system uses a Yb-doped ultrafast fiber laser. A GaBiAs based emitter antenna is used for THz emission. For THz detection, the system uses EO sampling method. Inside the system, THz beam is guided by two off-axis parabolic antennas and two teflon lenses on each side. Focal point at the prism base has a radius of 2.5 mm and the system has a SNR of 1000:1 with a bandwidth of 0.65 THz.

As a result of the ease of use provided by the THz ATR-TDS method, samples are measured by placing them on top of the prism same as the first system. One important factor is to make sure samples are completely in contact with the prism surface and there is no air gap in between. Sample placement accuracy and penetration depth are also important for the measurements with second system as well. The narrowness of the THz bandwidth of the system resulted in only time domain analysis of measurement results. Extracting optical properties with such a narrow bandwidth yields incorrect results. However, THz ATR-TDS method is useful even for time domain analysis of samples as shown in literature. Time domain measurements results show that the system and the ATR method again serve their purpose. THz signal is not lost to absorption caused by the water contained inside the samples. This result shows that a THz ATR-TDS system can be used for optical analysis of biological samples in THz range without needing specific sample preparation techniques. In addition, differences in measurements could be attributed to infected tissue amounts and their

types. A comparison with a healthy tissue sample could have been more helpful in this aspect but not being able to receive healthy samples prevents making strong comments. Finally, quality of the measurements can be improved by again optimizing the system and increasing system bandwidth. With an increased bandwidth and higher SNR, the system will have an increased spatial resolution which, in the end, will result in more detailed analysis and extraction of optical properties.

REFERENCES

[1] F. Sizov, "Brief history of thz and ir technologies," *Semiconductor physics quantum electronics & optoelectronics*, no. 22,№ 1, pp. 67–79, 2019.

[2] C. I. Eric R. Mueller, "Terahertz radiation sources for imaging and sensing applications," Nov 2006.

[3] BATOP, "Instruction manual and data sheet pca-40-05-10-1550." https://www.batop.de/products/terahertz/photoconductive-antenna/data-sheet/manual_PCA-40-05-10-1550.pdf Last Accessed: 2021/05/20.

[4] BATOP, "Instruction manual and data sheet pca-100-05-10-1550." https://www.batop.de/products/terahertz/photoconductive-antenna/data-sheet/manual_bPCA-100-05-10-1550.pdf Last Accessed: 2021/05/20.

[5] W. Herschel, "Xiv. experiments on the refrangibility of the invisible rays of the sun," *Philosophical Transactions of the Royal Society of London*, no. 90, pp. 284–292, 1800.

[6] J. W. Ritter, "Auffindung nicht sichtbarer sonnenstrahlen außerhalb des farbenspectrums, an der seite des viotets," *Ann Physik*, vol. 7, pp. 501–528, 1801.

[7] P. Shumyatsky and R. R. Alfano, "Terahertz sources," *Journal of biomedical optics*, vol. 16, no. 3, p. 033001, 2011.

[8] W. H. Hayt Jr, J. A. Buck, and M. J. Akhtar, *Engineering Electromagnetics| (SIE)*. McGraw-Hill Education, 2020.

[9] S. L. Dexheimer, *Terahertz spectroscopy: principles and applications*. CRC press, 2017.

[10] "Terahertz (thz) technology:an introduction and research update." High Frequency Electronics, February 2008.

[11] X.-C. Zhang and J. Xu, *Introduction to THz wave photonics*, vol. 29. Springer, 2010.

[12] E. Nichols and J. Tear, "Joining the infra-red and electric wave spectra," *The Astrophysical Journal*, vol. 61, p. 17, 1925.

[13] P. K. Sethy, P. R. Mishra, and S. Behera, "An introduction to terahertz technology, its history, properties and application," in *International conference on computing and communication*, 2015.

[14] X. Zhang, "Terahertz wave imaging: horizons and hurdles," *Physics in Medicine & Biology*, vol. 47, no. 21, p. 3667, 2002.

[15] B. B. Hu and M. C. Nuss, "Imaging with terahertz waves," *Optics letters*, vol. 20, no. 16, pp. 1716–1718, 1995.

[16] L. V. Titova, A. K. Ayesheshim, A. Golubov, R. Rodriguez-Juarez, R. Woycicki, F. A. Hegmann, and O. Kovalchuk, "Intense thz pulses down-regulate genes associated with skin cancer and psoriasis: a new therapeutic avenue?," *Scientific reports*, vol. 3, no. 1, pp. 1–6, 2013.

[17] G.-S. Park, Y. H. Kim, H. Han, J. K. Han, J. Ahn, J.-H. Son, W.-Y. Park, and Y. U. Jeong, *Convergence of Terahertz Sciences in Biomedical Systems*. Springer, 2012.

[18] Y. Sun, M. Y. Sy, Y.-X. J. Wang, A. T. Ahuja, Y.-T. Zhang, and E. Pickwell-MacPherson, "A promising diagnostic method: Terahertz pulsed imaging and spectroscopy," *World journal of radiology*, vol. 3, no. 3, p. 55, 2011.

[19] I. Wilke and S. Sengupta, "Nonlinear optical techniques for terahertz pulse generation and detection—optical rectication and electrooptic sampling," in *Terahertz Spectroscopy*, pp. 59–90, CRC press, 2017.

[20] N. Sellers, *Handbook of Terahertz Technology*. Scientific e-Resources, 2018.

[21] S. Kono, P. Gu, M. Tani, and K. Sakai, "Temperature dependence of terahertz radiation from n-type insb and n-type inas surfaces," *Applied Physics B*, vol. 71, no. 6, pp. 901–904, 2000.

[22] V. Apostolopoulos and M. Barnes, "Thz emitters based on the photo-dember effect," *Journal of Physics D: Applied Physics*, vol. 47, no. 37, p. 374002, 2014.

[23] A. Nahata and T. F. Heinz, "Generation of subpicosecond electrical pulses by optical rectification," *Optics letters*, vol. 23, no. 11, pp. 867–869, 1998.

[24] A. Rice, Y. Jin, X. Ma, X.-C. Zhang, D. Bliss, J. Larkin, and M. Alexander, "Terahertz optical rectification from< 110> zinc-blende crystals," *Applied physics letters*, vol. 64, no. 11, pp. 1324–1326, 1994.

[25] P. R. Smith, D. H. Auston, and M. C. Nuss, "Subpicosecond photoconducting dipole antennas," *IEEE Journal of Quantum Electronics*, vol. 24, no. 2, pp. 255–260, 1988.

[26] A. Rogalski and M. Razeghi, "Semiconductor ultraviolet photodetectors," *Opto-Electronics Review*, vol. 1996, no. 1-2, pp. 13–30, 1996.

[27] W. L. Chan, J. Deibel, and D. M. Mittleman, "Imaging with terahertz radiation," *Reports on progress in physics*, vol. 70, no. 8, p. 1325, 2007.

[28] M. Tani, M. Herrmann, and K. Sakai, "Generation and detection of terahertz pulsed radiation with photoconductive antennas and its application to imaging," *Measurement science and technology*, vol. 13, no. 11, p. 1739, 2002.

[29] P. U. Jepsen, D. G. Cooke, and M. Koch, "Terahertz spectroscopy and imaging–modern techniques and applications," *Laser & Photonics Reviews*, vol. 5, no. 1, pp. 124–166, 2011.

[30] D. Grischkowsky, S. Keiding, M. Van Exter, and C. Fattinger, "Far-infrared time-domain spectroscopy with terahertz beams of dielectrics and semiconductors," *JOSA B*, vol. 7, no. 10, pp. 2006–2015, 1990.

[31] J. B. Baxter and G. W. Guglietta, "Terahertz spectroscopy," *Analytical chemistry*, vol. 83, no. 12, pp. 4342–4368, 2011.

[32] O. Svelto, D. C. Hanna, *et al.*, *Principles of lasers*. Springer, 2010.

[33] P. U. Jepsen and H. Merbold, "Terahertz reflection spectroscopy of aqueous nacl and licl solutions," *Journal of Infrared, Millimeter, and Terahertz Waves*, vol. 31, no. 4, pp. 430–440, 2010.

[34] E. Arik, H. Altan, and O. Esenturk, "Dielectric properties of diesel and gasoline by terahertz spectroscopy," *Journal of Infrared, Millimeter, and Terahertz Waves*, vol. 35, no. 9, pp. 759–769, 2014.

[35] R. Ulbricht, E. Hendry, J. Shan, T. F. Heinz, and M. Bonn, "Carrier dynamics in semiconductors studied with time-resolved terahertz spectroscopy," *Reviews of Modern Physics*, vol. 83, no. 2, p. 543, 2011.

[36] K. Ohta and R. Iwamoto, "Experimental proof of the relation between thickness of the probed surface layer and absorbance in ft-ir/atr spectroscopy," *Applied spectroscopy*, vol. 39, no. 3, pp. 418–425, 1985.

[37] H. Hirori, K. Yamashita, M. Nagai, and K. Tanaka, "Attenuated total reflection spectroscopy in time domain using terahertz coherent pulses," *Japanese journal of applied physics*, vol. 43, no. 10A, p. L1287, 2004.

[38] U. Møller, D. G. Cooke, K. Tanaka, and P. U. Jepsen, "Terahertz reflection spectroscopy of debye relaxation in polar liquids," *JOSA B*, vol. 26, no. 9, pp. A113–A125, 2009.

[39] H. Yada, M. Nagai, and K. Tanaka, "Origin of the fast relaxation component of water and heavy water revealed by terahertz time-domain attenuated total reflection spectroscopy," *Chemical Physics Letters*, vol. 464, no. 4-6, pp. 166–170, 2008.

[40] K. Shiraga, Y. Ogawa, T. Suzuki, N. Kondo, A. Irisawa, and M. Imamura, "Determination of the complex dielectric constant of an epithelial cell monolayer in the terahertz region," *Applied physics letters*, vol. 102, no. 5, p. 053702, 2013.

[41] M. Nagai, H. Yada, T. Arikawa, and K. Tanaka, "Terahertz time-domain attenuated total reflection spectroscopy in water and biological solution," *International journal of infrared and millimeter waves*, vol. 27, no. 4, pp. 505–515, 2006.

[42] K. Sasaki, M. Mizuno, K. Wake, and S. Watanabe, "Monte carlo simulations of skin exposure to electromagnetic field from 10 ghz to 1 thz," *Physics in Medicine & Biology*, vol. 62, no. 17, p. 6993, 2017.

[43] N. Palka, M. Szala, and E. Czerwinska, "Characterization of prospective explosive materials using terahertz time-domain spectroscopy," *Applied optics*, vol. 55, no. 17, pp. 4575–4583, 2016.

[44] A. Nakanishi, Y. Kawada, T. Yasuda, K. Akiyama, and H. Takahashi, "Terahertz time domain attenuated total reflection spectroscopy with an integrated prism system," *Review of Scientific Instruments*, vol. 83, no. 3, p. 033103, 2012.

[45] A. Soltani, D. Jahn, L. Duschek, E. Castro-Camus, M. Koch, and W. Withayachumnankul, "Attenuated total reflection terahertz time-domain spectroscopy: uncertainty analysis and reduction scheme," *IEEE Transactions on Terahertz Science and Technology*, vol. 6, no. 1, pp. 32–39, 2016.

[46] O. Cherkasova, M. Nazarov, A. Angeluts, and A. Shkurinov, "Analysis of blood plasma at terahertz frequencies," *Optics and Spectroscopy*, vol. 120, no. 1, pp. 50–57, 2016.

[47] A. Fitzgerald, E. Berry, N. Zinov'ev, G. Walker, M. Smith, and J. M. Chamberlain, "An introduction to medical imaging with coherent terahertz frequency radiation.," *Physics in medicine and biology*, vol. 47 7, pp. R67–84, 2002.

[48] P. Han, M. Tani, M. Usami, S. Kono, R. Kersting, and X.-C. Zhang, "A direct comparison between terahertz time-domain spectroscopy and far-infrared fourier transform spectroscopy," *Journal of Applied Physics*, vol. 89, no. 4, pp. 2357–2359, 2001.

[49] N. Harrick and K. Beckmann, "Internal reflection spectroscopy," in *Characterization of Solid Surfaces*, pp. 215–245, Springer, 1974.

[50] M. Milosevic, *Internal reflection and ATR spectroscopy*, vol. 176. John Wiley & Sons, 2012.

[51] D. J. Griffiths, *Introduction to electrodynamics*. Prentice Hall New Jersey, 1962.

[52] A. Wojdyla and G. Gallot, "Attenuated internal reflection terahertz imaging," *Optics Letters*, vol. 38, no. 2, pp. 112–114, 2013.

[53] M. Van Exter and D. Grischkowsky, "Optical and electronic properties of doped

silicon from 0.1 to 2 thz," *Applied Physics Letters*, vol. 56, no. 17, pp. 1694–1696, 1990.

[54] B. Karagöz, "Pulsed three dimensional thz imaging," Master's thesis, Middle East Technical University, 2016.

[55] J.-L. Coutaz, F. Garet, and V. P. Wallace, *Principles of Terahertz time-domain spectroscopy: an introductory textbook*. CRC Press, 2018.

[56] H. Liu, Y. Wang, D. Xu, Z. Jiang, J. Li, L. Wu, C. Yan, L. Tang, Y. He, D. Yan, *et al.*, "Optimization for vertically scanning terahertz attenuated total reflection imaging," *Optics express*, vol. 26, no. 16, pp. 20744–20757, 2018.

[57] P. U. Jepsen, U. Møller, and H. Merbold, "Investigation of aqueous alcohol and sugar solutions with reflection terahertz time-domain spectroscopy," *Optics Express*, vol. 15, no. 22, pp. 14717–14737, 2007.

[58] D. S. Venables and C. A. Schmuttenmaer, "Spectroscopy and dynamics of mixtures of water with acetone, acetonitrile, and methanol," *The Journal of Chemical Physics*, vol. 113, no. 24, pp. 11222–11236, 2000.

[59] O. Cherkasova, M. Nazarov, and A. Shkurinov, "Noninvasive blood glucose monitoring in the terahertz frequency range," *Optical and Quantum Electronics*, vol. 48, no. 3, p. 217, 2016.

[60] D. A. Newnham and P. F. Taday, "Pulsed terahertz attenuated total reflection spectroscopy," *Applied spectroscopy*, vol. 62, no. 4, pp. 394–398, 2008.

APPENDIX A

MATLAB CODE FOR DATA ANALYSIS

```
format long
nair = 1;
nprism = 3.42;                  %Refractive index of Si prism.
a= 51.6;                        %Incidence angle to prism base.
c = 3*10^8;                     %Speed of light in vacuum
[R] = dlmread('','\t');         %THIS IS FOR REFERENCE MEASUREMENT
[S] = dlmread('','\t');         %THIS IS FOR SAMPLE MEASUREMENT
V2 = S(:,2);                    % Data Channel (SAMPLE)
V = R(:,2);                     % Data Channel (REFERENCE)
Z = R(:,1);                     %Time Channel  (BOTH)


Ts = mean(diff(Z));             % Sampling Interval
Fs = 1/Ts;                      % Sampling Frequency
Fn = Fs/2;                      % Excitation Frequency
LF = size(V,1);                 % Length of Data Vector
T = linspace(0,1,LF)*Ts;        % Create Time Vector
FF = fftshift(fft(V)/LF);       % FFT of Reference Data
FF2 = fftshift(fft(V2)/LF);     % FFT of Sample Data
FShift =(-LF/2:LF/2-1)*(Fs/LF); % Shifts FFT

I = imag(FF);                   % Imag. Part of Reference FFT
R = real(FF);                   % Real Part of  Reference FFT
```

```
Mag = sqrt(I.^2+R.^2);              %Magnitude of complex FFT
Amp = Mag/(LF/2);                   %Amplitude of complex FFT
PMSA = 0.5*(Amp).^2;                %Power Mean Square Amplitude
dB = 20*log10(Amp);                 %Power dB

Phase = angle(FF);                  %Phase of FFT
UnwPhase = unwrap(Phase);           %Unwraps Phase
Ang = rad2deg(UnwPhase);            %Converts Phase to angle

I2 = imag(FF2);                     % Imag. Part of Sample FFT
R2 = real(FF2);                     % Real Part of Sample FFT

Mag2= sqrt(I2.^2+R2.^2);     %
Amp2 = Mag2/(LF/2);          %
PMSA2 = 0.5*(Amp2).^2;       %
dB2 = 20*log10(Amp2);        %THESE DO THE SAME THING AS BEFORE
                             %
Phase2 = angle(FF2);         %
UnwPhase2 = unwrap(Phase2); %
Ang2 = rad2deg(UnwPhase2);   %


plot(FShift,Ang)             %Unwrapped Reference Phase Plot
grid
xlabel("Frequency")
ylabel("Unwrapped Phase of Reference")
title("Reference Unwrapped Phase vs Frequency")
xlim([-1 1])

plot(FShift,Ang2)            %Unwrapped Sample Phase Plot
grid
xlabel("Frequency")
ylabel("Unwrapped Phase of Sample")
```

```
title("Sample Unwrapped Phase vs Frequency")
xlim([-1 1])

TPowR = PMSA2./PMSA;         %Find Measurement Range
plot(FShift,TPowR)           %Plot Measurement Range
grid
xlabel("Frequency")
ylabel("Power Transmission")
title("Transmission vs Frequency")
xlim([0.1 0.9])

%%%%%%%%%%%%%%%%%%% ATR DATA ANALYSIS %%%%%%%%%%%%%%%%%%%%%%%%

FFTR =FF2./FF;              %Ratio of Sample and Reference FFT

%%%%%%%%%Fresnell Coefficient of air-prism interface %%%%%%%%%%

rr = -(nair*cosd(a)+nprism*(sqrt(1-(nprism)^2*(sind(a))^2)))
    /(nair*cosd(a)+nprism*(sqrt((1-(nprism)^2*(sind(a))^2)));

%%%%%%%%%%%%%%%%%%%%%%%%%%%%%%%%%%%%%%%%%%%%%%%%%%%%%%%%%%%%%%%

Term1=(cosd(a)/3.42);
Term2=(FFTR*rr);
Term3=1-Term2;
Term4=1+Term2;

phi = Term1*(Term3./Term4);
iphi = 1./phi;

%Calculates refractive index with + sign
nsp=(iphi).*(sqrt(0.5*(1+sqrt(1-(2.*phi*nprism.*(cosd(a))^2)))));
```

```
%Calculates Refractive index with - sign
nsn=(iphi).*(sqrt(0.5*(1-sqrt(1-(2.*phi*nprism.*(cosd(a))^2)))));


for l = 1:numel(nsp)
    if imag(nsp(l))>0
      espx(l) = nsn(l);
    else                    %Results with negative imag. part.
      espx(l) = nsp(l);
    end
end

esp = espx.';

nR = real(esp);
                  %Real and Imag. parts of the refractive index.
nI = imag(nsn);

plot(FShift,nR) %Plots n wrt Frequency.
grid
xlabel('Frequency (THz)')
ylabel('n')
title("Refractive Index vs Frequency")
xlim([0.1 1])


plot(FShift,nI) %Plots k wrt Frequency.
grid
xlabel('Frequency (THz)')
ylabel('k')
title("Extinction Coefficient vs Frequency")
xlim([0.1 1])
```

```
%Calculates absorption coefficient of sample.
Abs = (4*pi*abs(nI).*FShift'*10^12)/(c*100);

%Plots Absorption coefficient wrt Frequency.
plot(FShift,Abs)
grid
xlabel('Frequency (THz)')
ylabel('Absorption (cm^-1)')
title("Absorption vs Frequency")
xlim([0.1 1])
```

APPENDIX B

MATLAB CODE FOR PLOTS IN CHAPTER 2

```
MinAngle = 0.01; %Minimum incidence angle in degrees.
MaxAngle = 89.99; %Maximum incidence angle in degrees.
MinFreq = 0.1*10^12; %Minimum Light Frequency in Hz
MaxFreq = 1*10^12; %Maximum Light Frequency in Hz
n2 = 3.42; % The denser mediun (Si-For Consistency)
n1 = 1; % The rarer medium (Air)
m = 3; %This number  can be changed to see penetration depth for
   %more or less number of frequencies between the range.
p = 100;
nsam = 2.15 %Refractive index of a sample
\end{matlabcode}
\begin{matlaboutput}
nsam = 2.1500
\end{matlaboutput}
\begin{matlabcode}
nsmax = 2.68;% Maximum measurable refractive index
nsmin = 1; % Minimum measurable refractive index
z = linspace(MinAngle,MaxAngle,270);
x = linspace(MinFreq,MaxFreq,m);
t = linspace(MinFreq,MaxFreq,p);
y = linspace(nsmin,nsmax,100);
g = linspace(2.1,2.3,3);
n  = n2/n1;
for l = 1:length(x)
```

```
    for k = 1:length(z)
    %Fresnel Coefficient r  for s-pol
    rs(k) = (n2*cosd(z(k))-sqrt(n1^2-n2^2*(sind(z(k)))^2))/(n2*cosd(z(k))
    +sqrt(n1^2-n2^2*(sind(z(k)))^2));
    %Fresnel Coefficient r for  p-pol.
    rp(k) = (n1^2*cosd(z(k))-n2*sqrt(n1^2-n2^2*(sind(z(k)))^2))/
    (n1^2*cosd(z(k))+n2*sqrt(n1^2-n2^2*(sind(z(k)))^2));
    %Reflection phase shift for p-pol.
    Pp(k) = 2*atand(n*(sqrt(n^2*(sind(z(k)))^2-1))/(cosd(z(k))));
    %Reflection phase shift for s-pol.
    Ps(k) = 2*atand((sqrt(n^2*(sind(z(k)))^2-1))/(n*cosd(z(k))));
    %Penetration depth wrt incidence angle in mm at 0.3, 0.6, 1 THz.
    Pd(l,k) = (3*10^8)/((2*pi*x(l))*sqrt(n2^2*(sind(z(k)))^2-n1^2))*10^3;
    end

    %Penetration depth in mm for samples from n=1 to n=2.68 at for 0.3,
    0.6, 1 THz.
    for m = 1:length(y)
    Pde(l,m) = (3*10^8)/((2*pi*x(l))*sqrt(n2^2*(sind(51.6))^2-
    (y(m))^2))*10^3;
    end
end
%Penetration depth for specific samples wrt. frequency
    for h = 1:length(t)
  Pdex(h) = (3*10^8)/((2*pi*t(h))*sqrt(n2^2*(sind(51.6))^2-
  (nsam)^2))*10^3;
    end
Rs = abs(rs.^2); %Reflectance R for S pol.
Rp = abs(rp.^2); %Reflectance R for p pol.
D = Pp-Ps; %Phase Shift Difference
plot(z,Rp,z,Rs)
grid
xlabel("Incidence Angle (deg)")
```

```
ylabel("Reflectance")
title("Reflectance for P and S Polarizations vs Incidence Angle")

plot(z,Pp,z,Ps,z,D)
grid
xlabel("Incidence Angle (deg)")
ylabel("Phase Change")
title("Phase Change of P and S Polarizations vs Incidence Angle")

plot(z,Pd)
grid
xlabel("Incidence Angle")
ylabel("Penetration Depth (mm)")
title("Penetration Depth vs Incidence Angle at 0.1, 0.5 and 1 THz")

plot(y,Pde)
grid
xlabel("Refractive Index")
ylabel("Penetration Depth (mm)")
title("Penetration Depth vs Ref. Index at 0.1, 0.5 and 1 THz")

plot(t/10^12,Pdex)
grid
xlabel("Frequency")
ylabel("Penetration Depth (mm)")
title("Penetration Depth vs Frequency for a Sample")

%Data below (left hand side) can directly be imported to Origin.
RsT=Rs';
RpT=Rp';
Ang=z';
PpT=Pp';
PsT=Ps';
```

```
PdT=Pd';
DT=D';
PdeT=Pde';
Ref=y';
S=Pdex';
d=(t/10^12)';
```